International Journal of Plasticity 151 (2022) 103179

Contents lists available at ScienceDirect

International Journal of Plasticity

journal homepage: www.elsevier.com/locate/ijplas

Simulation of the response and evolution of localization in pseudoelastic NiTi tubes under biaxial stress states

Karlos Kazinakis, Stelios Kyriakides *, Chad M. Landis

Research Center for Mechanics of Solids, Structures & Materials, ASE, The University of Texas at Austin, Austin, Texas 78712, United States

ARTICLE INFO

Keywords:
Combined internal pressure-axial load
Biaxial stress
NiTi tubes
Pseudoelasticity
Inhomogeneous deformation
Modeling

ABSTRACT

The well-known tension/compression asymmetry exhibited by nearly equiatomic NiTi has been previously modeled using a hardening potential for compression and a partially softening one for tension to represent pseudoelastic phase transformations (Jiang et al., 2016b). The present study first extends this constitutive model to include anisotropy revealed in the combined axial force-internal pressure experiments on NiTi tubes of Bechle and Kyriakides (2016a). The model is then calibrated anew, implemented in a finite element analysis of tubes and used to simulate the entire range of biaxial experiments performed. Overall, the simulations reproduce well the stress-average strain hystereses and the transformation stress loci, while for hoop dominant stress paths the extents of the transformation strains are somewhat over-predicted. The evolution of localization in the form of high or low strain helical bands, the variation of helix angles with respect to the stress ratio, and the dissipated energy compare favorably. The hardening response and essentially homogeneous deformation exhibited in the neighborhood of the equibiaxial stress state is reproduced, but with reduced hardening and mild inhomogeneity. Despite some minor differences, the results demonstrate the overall success of the analysis in reproducing the phenomena-rich behavior exhibited by tubular NiTi structures under biaxial loadings.

1. Introduction

Nearly equiatomic NiTi can be strained at room temperature to several percent and fully recover upon unloading, called *pseudoelastic* behavior. This property is derived from solid-state transformations between the *austenitic* (A) and *martensitic* (M) phases and as a result the load-unload response of the material traces a closed stress-strain hysteresis. Under tension, the reversible transformation results in inhomogeneous deformation with the hysteresis exhibiting an upper and a lower stress plateau during which the two phases co-exist (e.g., Shaw and Kyriakides, 1995,1997; Liu et al., 1999; Iadicola and Shaw, 2002; Mao et al., 2010; Li and Sun, 2002; Daly et al., 2007; Bechle and Kyriakides, 2014; Reedlunn et al., 2014). In contrast, under compression the transformation leads to a monotonic hysteresis with higher stress, lower strain, and essentially homogeneous deformation (e.g., Jacobus et al., 1996; Orgeas and Favier, 1998; Bechle and Kyriakides, 2014; Reedlunn et al., 2014; Elibol et al., 2015). More complex manifestations of the tension/compression asymmetry became apparent in biaxial experiments on pseudoelastic NiTi tubes under combined axial force and torsional loadings (e.g., Helm and Haupt, 2001; Sun and Li, 2002; Yu et al., 2015; Reedlunn et al., 2020) and axial force-internal pressure (e.g., Bechle and Kyriakides, 2016a, 2016b).

The axial force-internal pressure biaxial experiments of Bechle and Kyriakides (2016a), which are the focus of the present study

* Corresponding author.
E-mail address: skk@mail.utexas.edu (S. Kyriakides).

https://doi.org/10.1016/j.ijplas.2021.103179
Received 1 November 2021; Received in revised form 9 December 2021;
Available online 27 December 2021

involved thin-walled tubes with diameter-to-thickness ratios (D/t) of about 25, tested under radial loading paths with nominal axial to hoop stress ratios $(\sigma_x/\sigma_\theta \equiv \alpha)$ ranging from -1.0 to uniaxial tension (∞). But for a narrow region near equibiaxial tension, transformation leads to localized helical deformation bands with helix angles and stress plateaus that depend on the stress ratio. In the vicinity of equibiaxial tension, the material reverted to hardening and nearly homogeneous deformation.

Biaxial experiments have also revealed anisotropy, apparently as a result of processing induced texture (e.g., Sun and Li, 2002; Bechle and Kyriakides, 2016a; Reedlunn et al., 2020). Thus, the loci of the transformation stresses of the axial force - internal pressure results trace an elongated trajectory along the equibiaxial direction with modest anisotropy. Interestingly, the transformation strains exhibit a more significant anisotropy between the axial and hoop dominant stress paths.

The tension/compression asymmetry, including the contrasting softening and hardening behavior alluded to above, plays a vital role in SMA structural behavior (e.g., Bechle and Kyriakides, 2014; Reedlunn et al., 2014; Jiang et al., 2016a, 2016b, 2017a, 2017b, 2017c; Kazinakis et al., 2021; Rezaee-Hajidehi and Stupkiewicz, 2021). Driven by these behaviors, Jiang et al. (2016b) and Jiang and Landis (2016) presented a phenomenological constitutive framework that incorporates the reversibility of transformation and the tension/compression asymmetry of pseudoelastic SMA behavior under isothermal conditions. The constitutive model was implemented in finite element analyses to successfully simulate the response, localization, buckling, and postbuckling behavior of tubular structures under tension, compression and bending.

The main objective of the present study is to examine the performance of the constitutive model under the more general biaxial stress states generated by the experiments of Bechle and Kyriakides (2016a, 2016b). In most of the axial force-internal pressure experiments reported, the reversible transformations resulted in localization in the form of spiral patterns. Simulation of this pattern-rich behavior requires treating the tubular specimens as structures. The model is extended to include anisotropy, calibrated anew, and implemented in a finite element analysis of tubes under combined axial force and internal pressure. The model tube is pressurized under volume control using incompressible fluid elements. The axial force required to achieve the desired radial stress ratio is then prescribed via a feedback loop. The performance of the analysis is evaluated by comparing the calculated responses and deformation patterns to the measured results.

In the way of motivating the study, the paper starts with a brief review of the main features of the experimental results – Section 2. The extended constitutive model and its calibration, followed by the finite element analysis are presented in Section 3. Results from a series of simulations with biaxiality ratios that span the range of the experiments $(-1 \leq \alpha \leq \infty)$ constitute the main thrust of the manuscript. The key aspects of the numerical results are discussed followed by the main conclusions from the work.

2. Review of biaxial experiments

The experiments of Bechle and Kyriakides (2016a) involved nearly equiatomic NiTi tubular stock (50.9 at% Ni) with outer diameter 6.35 mm and wall thickness of 0.25 mm $(D/t = 25.0)$. The material transformation temperatures were $\{A_s, A_f\} = \{-10,\ 12\}$ °C and the experiments were performed at 23 °C – in the pseudoelastic regime. Specimens 114 mm long were cut from longer tubular stock and inserted in aligned axisymmetric grips leaving a 50 mm test section which had been previously speckled for Digital Image Correlation (DIC). The specimens were loaded under combined internal pressure (P) and axial force (F) tracing radial paths in the axial-hoop stress space such that

$$\sigma_x = \alpha\sigma_\theta,\ \ \alpha = \text{const.} \tag{1a}$$

The two stresses are related to the loads by

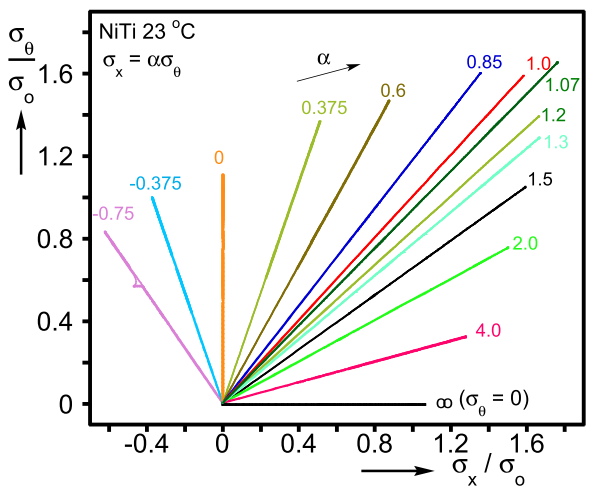

Fig. 1. Prescribed axial-hoop stress radial paths from representative experiments on NiTi tubes from Bechle and Kyriakides (2016a).

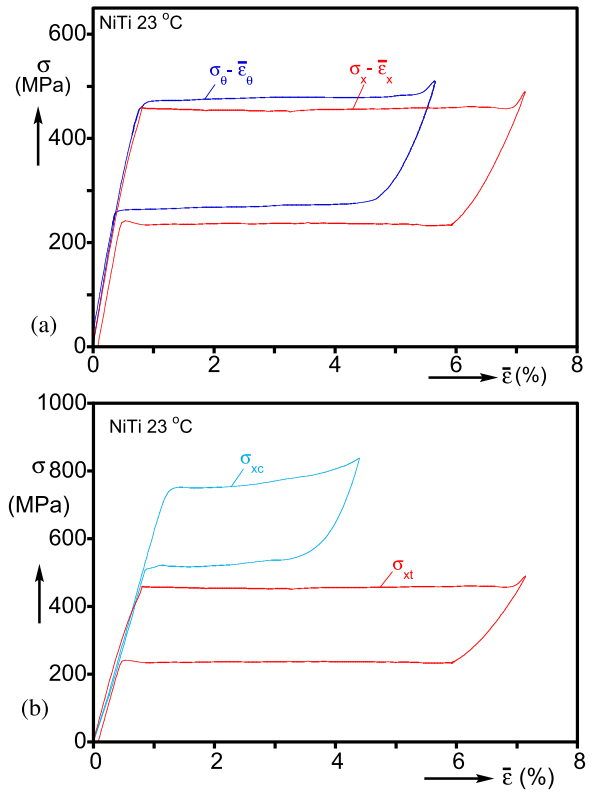

Fig. 2. (a) Comparison between the uniaxial tensile stress-average strain response measured in the axial and hoop directions – an illustration of anisotropy. (b) Comparison between the axial stress-average strain response in tension and compression – an illustration of the tension/compression asymmetry in NiTi.

$$\sigma_x = \frac{F}{2\pi Rt} + \frac{PR}{2t} \quad \text{and} \quad \sigma_\theta = \frac{PR}{t} \tag{1b}$$

Pressure was applied by prescribing a fluid flux into the closed system using a precision syringe pump (*volume control*). The testing machine was run under load control and the two loads were connected through feedback with the pressure signal as the external command. As the pressure gradually increases, the feedback enables the testing machine to apply the force required to keep the two stresses at the required ratio. Stereo DIC provided a full-field monitoring of the deformation of the test section. The strain fields $\{\varepsilon_x, \varepsilon_\theta\}$ were established by post-processing of the images and related to the corresponding stresses. Results from 26 experiments for $-1.0 \leq \alpha \leq \infty$ are reported in Table 1 of Bechle and Kyriakides (2016a). Fig. 1 plots the stress paths traced for a representative set of cases that are simulated here.

We start with Fig. 2a that compares the nominal stress-average strain responses for the two uniaxial loading cases in the axial ($\alpha = \infty$) and hoop ($\alpha = 0$) directions. Both trace closed stress hystereses with plateaus during which the A→M transformation occurs during loading and the M→A on unloading. During the plateaus, the deformation is highly inhomogeneous developing spiral bands of transformed M oriented at about 29.1° for the hoop and 55.8° for the axial test. As the specimen unloads, the transformation propagates primarily via multi-pronged bands. The elastic moduli have slightly different values, and the transformation stresses (stress plateaus) are somewhat higher for the hoop response than the axial one. Even more pronounced differences are observed in the extents of the stress plateaus with the upper plateau being about 25% smaller for the hoop response. Both of these differences are indications that, in addition to the tension-compression asymmetry reported in Bechle and Kyriakides (2014), the material exhibits anisotropy. (The tension-compression asymmetry for the present material is demonstrated Fig. 2b).

The main features of the biaxial experimental results will be outlined using results for $\alpha = 0.375$, 1.0 and 4.0.

Experiment $\sigma_x = 0.375\sigma_\theta$

Fig. 3a shows the nominal stress-average strain responses recorded in the axial and hoop directions. Twenty axial and hoop strain contours corresponding to the DIC field of view (FOV) that match the numbered bullets on the responses are shown in Fig. 3b. The two responses trace closed hystereses with the $\sigma_\theta - \overline{\varepsilon}_\theta$ being significantly larger. The axial strain is negative as it is dominated by the Poisson's effect. Deformation remains uniform until transformation to M commences when the two responses develop gradual stress knees followed by stress plateaus. A sharp tipped band of martensite at an angle of 32.7° to the axis of the tube has entered the FOV in

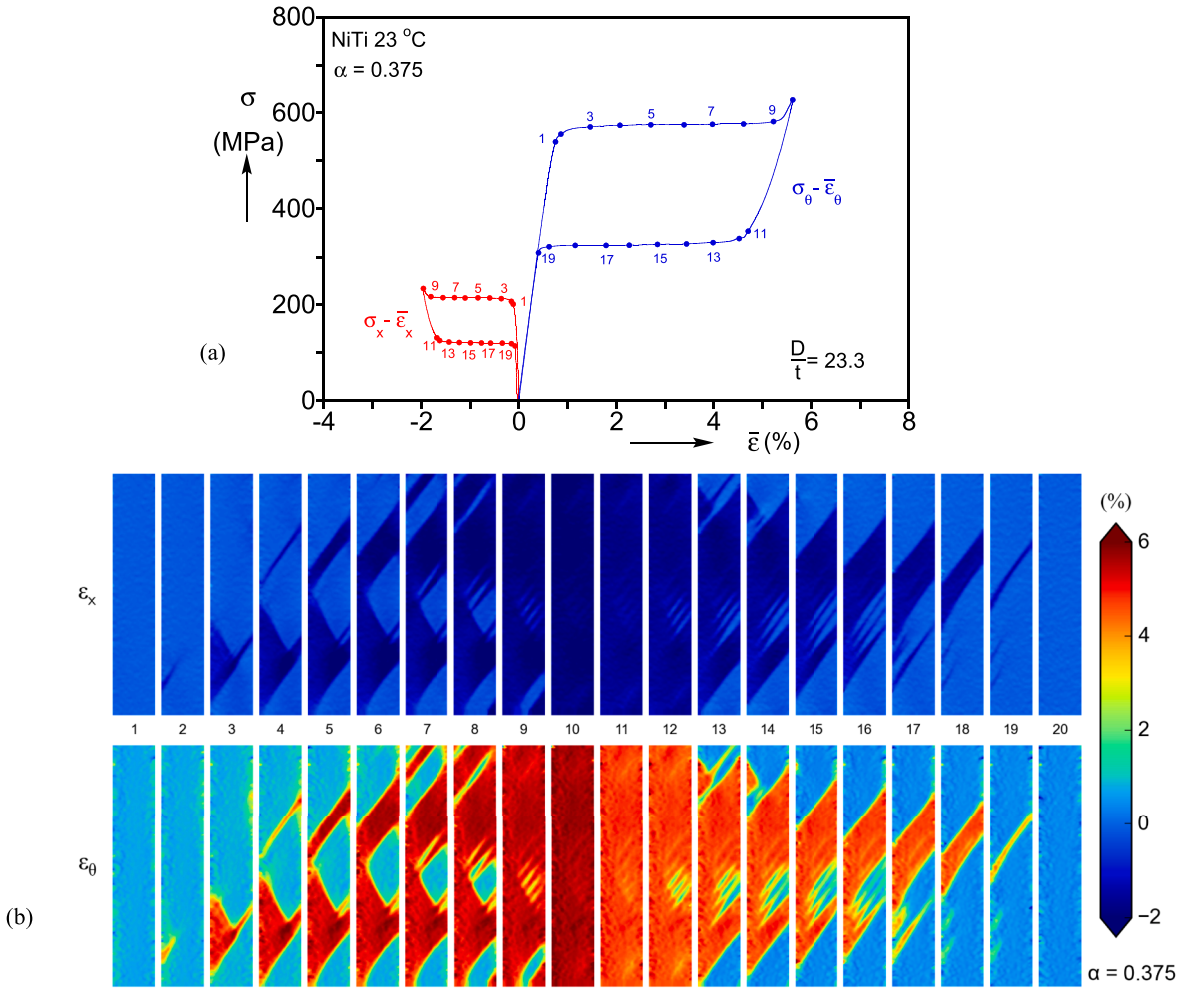

Fig. 3. (a) Measured stress-average strain responses recorded in biaxial test $\sigma_x = 0.375\sigma_\theta$. (b) Sequences of axial and hoop strain contours from DIC corresponding to the numbered bullets marked on the responses in (a) (from Bechle and Kyriakides, 2016a).

image ②. By ③ the transformed material with hoop strain of about 5% has evolved into a triangular island while the rest of the domain remains at 0.85% – strain at the initial stress knee. Subsequently, this island of M grows and a second helical band of higher strain enters the FOV from the top in image ④. The two transformed zones grow and coalesce leaving a diamond shaped island of A near mid-height – images ⑤ and ⑥. The upper zone of transformation grows while the lower grows less. In image ⑦ a new narrow band of higher strain has appeared at the top. It is noteworthy that bands and zones of transformed material have the same orientation. Beyond point ⑨, most of the remaining islands of A have transformed, the stress takes an upswing and deformation in image ⑩ becomes uniform.

The martensitic phase unloads uniformly until station ⑪. A knee forms as M→A transformation initiates with A taking the strain at the end of the lower hoop plateau (~0.39%). In image ⑫ the A zones are narrow islands of lower strain at the sites that were the last to transform to M. The stress stabilizes to a plateau as additional transformation fronts appear first at the top and then at the bottom of the FOV with zones that transformed late to M taking priority. Once more, all transformation zones and fronts have the same orientation. In image ⑬ a triangular island of A has formed at the bottom and a nearly V-shaped one at the top. In images ⑮ and ⑯ these two zones have propagated towards the center with clear inclined fronts. Simultaneously, the central striped islands of A have started growing so that by image ⑰ a single inclined zone of M remains. It continues to narrow until in image ⑲ it has been reduced to a single narrow band. Transformation is completed with the hysteresis closing, and further unloading is along the loading trajectory. By and large this behavior is representative of that observed for stress ratios $-1 \leq \alpha < 0.85$ with, however, different spiral angles.

Experiment $\sigma_x = 1.0\sigma_\theta$

Fig. 4 shows the nominal stress-average strain responses for the equibiaxial case together with a set of corresponding DIC images of the deformation in the FOV. The behavior is distinctly different from the two uniaxial results and those of $\alpha = 0.375$. Here the stresses

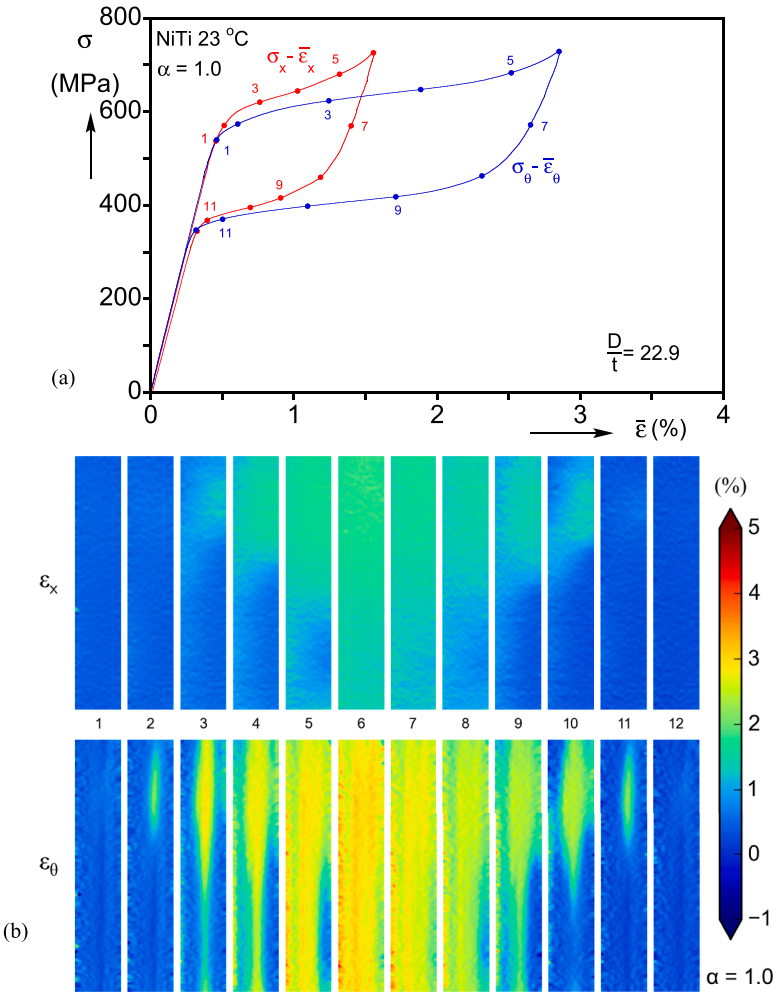

Fig. 4. (a) Measured stress-average strain responses recorded in biaxial test $\sigma_x = 1.0\sigma_\theta$. (b) Sequences of axial and hoop strain contours from DIC corresponding to the numbered bullets marked on the responses in (a) (from Bechle and Kyriakides, 2016a).

increase monotonically, the transformation strains are smaller, and the hystereses are closed but enclose much smaller areas. Furthermore, despite the equibiaxial state of stress the axial strain is less than half that of the hoop strain. The hoop strain contours exhibit very mild, diffuse localization with an axial orientation (see images ② to ④). In image ⑤ and ⑥ the weak axial bands broaden and cover the whole FOV. In the axial strain contours inhomogeneity or preferred orientation are not discernable at the scale of this strain resolution. Unloading produces the reverse deformation patterns with both strains fully recovered.

This behavior of monotonically increasing responses with smaller strain extents with limited diffuse localization is characteristic of the zone covering $0.85 \leq \alpha < 1.2$. As will be demonstrated in the analysis, this behavior is a consequence of the monotonic nature of the uniaxial compressive response. In the case of $\alpha = 1.07$, the responses were also monotonic, however, the axial response became dominant. Consequently, the two hystereses are expected to have the same size for a biaxiality ratio between 1.0 and 1.07, all manifestations of the underlying anisotropy.

Experiment $\sigma_x = 4.0\sigma_\theta$

Fig. 5 summarizes results for the axial stress dominant path of $\alpha = 4.0$ that is representative of the results for paths with $1.5 < \alpha < 8.0$. The responses (Fig. 5a) trace closed hystereses with rather sharp transition stress knees followed by relatively flat plateaus for both loading and unloading; both similar to the uniaxial tension behavior. In image ② (Fig. 5b) just after the onset of transformation, a sinistral helical band with axial strain of about 7% starts at the upper end, and wraps around the specimen with its pointed front appearing in the FOV. It has an inclination of 60° to the axis of the tube. In image ③ the helical band propagates one more time around the specimen, while simultaneously broadening behind its tip. In image ④ the band widens further and its front has reached the lower edge of the FOV. Subsequently, transformation takes place by widening of the now stationary band as seen in image ⑤, and is completed by image ⑦.

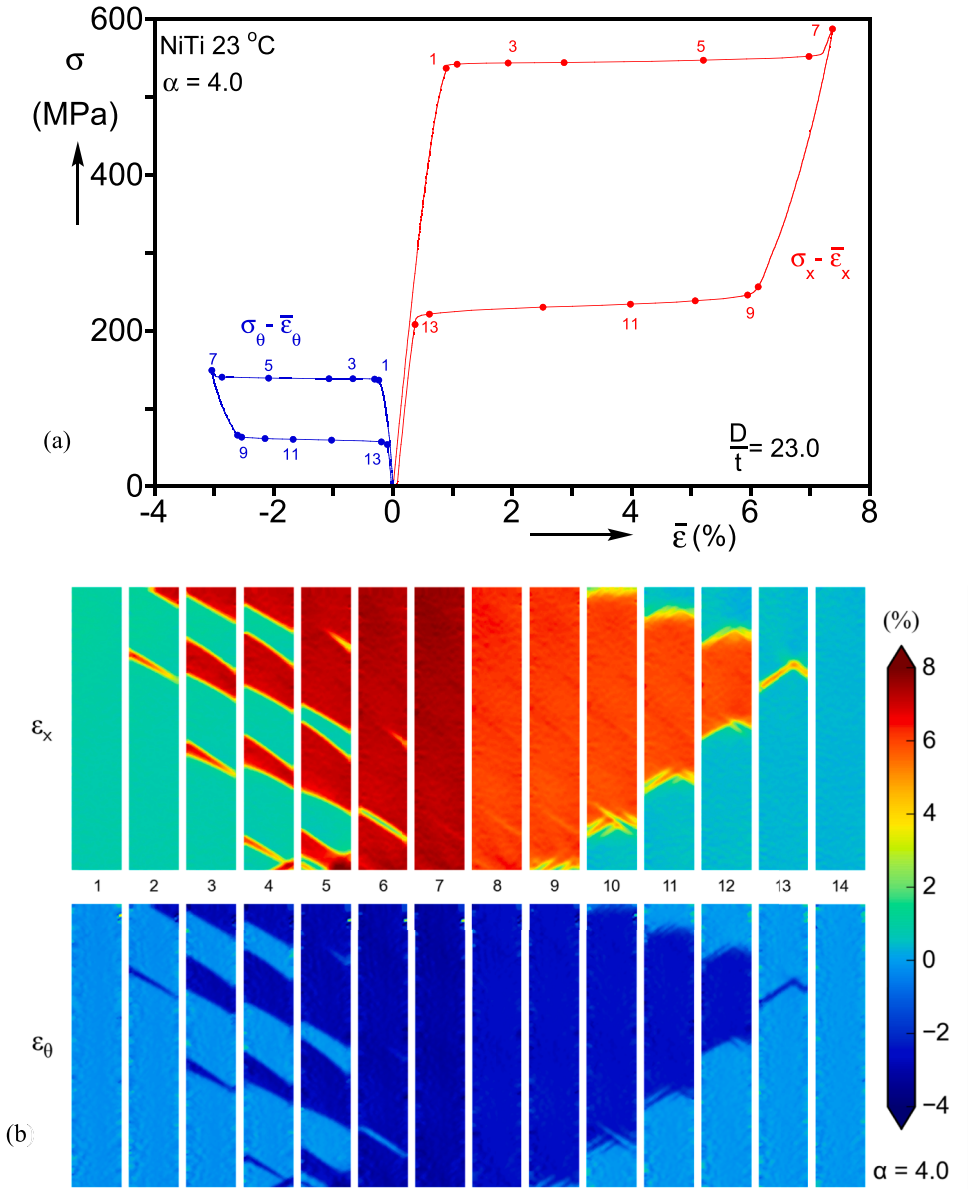

Fig. 5. (a) Measured stress-average strain responses recorded in biaxial test $\sigma_x = 4.0\sigma_\theta$. (b) Sequences of axial and hoop strain contours from DIC corresponding to the numbered bullets marked on the responses in (a) (from Bechle and Kyriakides, 2016a).

The specimen, mainly in the martensitic phase, unloads uniformly until station ⑧. A dextral multi-helical front of A enters the FOV at the lower end just before image ⑨. It propagates upwards developing into a front with helixes of both chiralities. In image ⑩ a second multi-helical front enters the FOV from the top. The two fronts of A propagate towards each other and in image ⑫ they have evolved into chevron-like patterns where transformation takes place along both characteristics. In image ⑬, but for a small sliver of M, the specimen has transformed back to A. We note that because of limitations of the volume-controlled loading scheme used, some heating of the specimen during the forward and cooling during the reverse transformation took place for experiments with $\alpha > 1.5$ (see Bechle and Kyriakides, 2016b). This is responsible for the small positive inclinations of the two stress-plateaus in Fig. 5a.

In summary, the results of the biaxial experiments revealed additional complexities of NiTi mechanical behavior. In addition to the previously reported tension/compression asymmetry, the material as processed exhibits anisotropy that influences both the stress and strain transformation surfaces. Fig. 6a plots the axial and hoop stress at the "nucleation" and "completion" of M and A for each of the 26 biaxial experiments together with fits generated as in Bechle and Kyriakides (2016a). The surfaces differ significantly from a Mises one as they are pointed along the equibiaxial tension direction and due to the anisotropy do not possess the reflection symmetry about $\alpha = 1.0$ direction (see comparison in Fig. 23 of the reference above and simultaneously reflect the anisotropy exhibited by the stresses). For loading paths with stress ratios $-1 \leq \alpha \leq 0.5$ and $1.8 \leq \alpha \leq \infty$ the A→M transformations traced relatively flat stress plateaus and

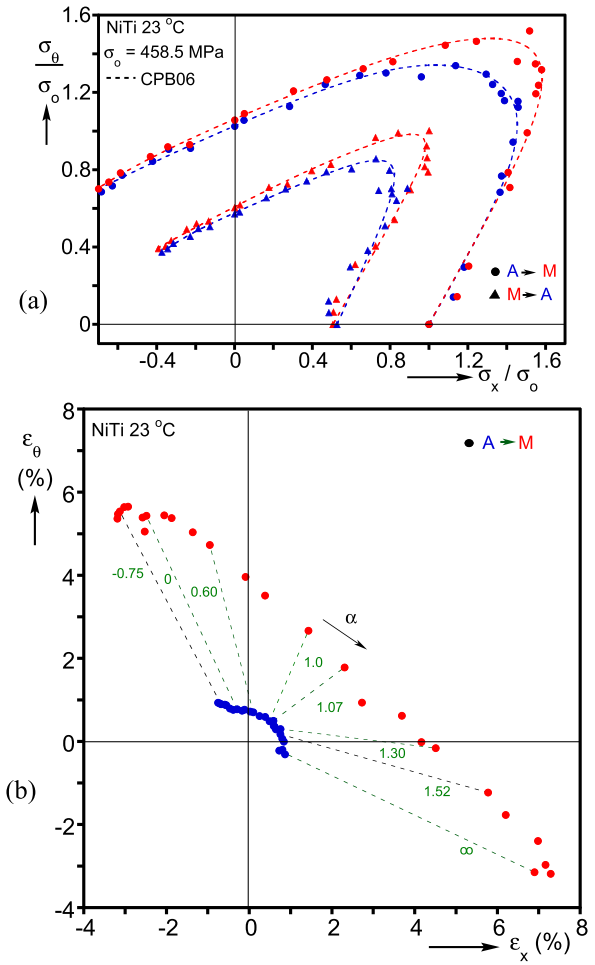

Fig. 6. (a) Loci of measured stresses at the "nucleation" and "completion" of M and A transformations and fitted surfaces. (b) Measured axial vs. hoop strains at the "nucleation" and "completion" of M transformation (from Bechle and Kyriakides, 2016a).

consequently the data at the onset and completion of transformation are closely spaced. Paths with $0.6 \leq \alpha \leq 1.0$ developed progressively increasing hardening while for $1.0 \leq \alpha < 1.8$ the hardening progressively decreased. Hardening increases the distance between the two critical stresses as demonstrated in Fig. 6a with the maximum distance being close to the equibiaxial case.

The effect of the tension/compression asymmetry and anisotropy on the A→M transformation strains is summarized in Fig. 6b, which plots the axial against the hoop strain at the "nucleation" and "completion" of M transformation. The difference in the transformation strains in uniaxial tension and pure hoop cases is clearly much more pronounced than the corresponding stresses. Furthermore, the extent of strain induced by the transformation has large values for the negative and larger positive values of α, and decreases as the equibiaxial stress state is approached from either side.

3. Analysis

A phenomenological constitutive model framework for NiTi in the pseudoelastic temperature regime has been presented in Jiang et al. (2016b) and Jiang and Landis (2016). The model is calibrated on the uniaxial tension and compression material response and its key features include the reversible nature of the A⇄M transformations using a single transformation surface along with kinematic hardening to capture the tension/compression asymmetry. The inhomogeneous deformation associated with tensile stress states is modeled by partially softening branches during loading and unloading (see Ericksen, 1975; Abeyaratne and Knowles, 2006; Shaw and Kyriakides, 1998; Kyriakides and Miller, 2000; Hallai and Kyriakides, 2013). The model was used to study the effect of the onset and evolution of phase transformations on simple structures that are primarily loaded under uniaxial tension or compression. They include tubes under compression (Jiang et al., 2016a; 2016b), under tension (Jiang et al., 2017a), and under bending (Jiang et al., 2017b; Kazinakis et al., 2021). The biaxial experiments summarized in Section 2 demonstrate that the behavior of the material under biaxial loadings is more complex than previously recognized. The role of the tension/compression asymmetry is more complicated, the material exhibits anisotropy in stress and strain, and the two phenomena are coupled. The aim of the analysis is to first extend the

constitutive model as dictated by the new data, and modify the associated UMAT. The performance of the constitutive model is then evaluated by implementing it into a finite element analysis that is used to simulate the whole range of biaxial experiments.

3.1. Constitutive model

The strain increment is decomposed into elastic and transformation components

$$\dot{\varepsilon}_{ij} = \dot{\varepsilon}^{e}_{ij} + \dot{\varepsilon}^{t}_{ij}. \tag{2}$$

The elastic deformation is isotropic with constants $\{E, \nu\}$ and related to the stress increment by

$$\dot{\sigma}_{ij} = C_{ijkl}\left(\dot{\varepsilon}_{kl} - \dot{\varepsilon}^{t}_{kl}\right). \tag{3}$$

The elastic deformation is enclosed by a transformation surface that obeys kinematic hardening defined by

$$\Phi = \frac{3}{2}\left(s_{ij} - s^{B}_{ij}\right)\left(s_{ij} - s^{B}_{ij}\right) - \sigma^{2}_{o} = 0, \tag{4}$$

where s_{ij} and s^{B}_{ij} are the deviatoric components of stress and back stress and σ_o represents the size of the transformation surface. The transformation strain increment follows an associated flow rule thus,

$$\dot{\varepsilon}^{t}_{ij} = \Lambda\left(s_{ij} - s^{B}_{ij}\right), \Lambda \geq 0. \tag{5}$$

The back stress is derived from a potential that depends only on the transformation strain

$$\sigma^{B}_{ij} = \frac{\partial \psi^{t}}{\partial \varepsilon^{t}_{ij}}. \tag{6}$$

The tension/compression asymmetry exhibited by this material is introduced by expressing this potential as a combination of a tensile and a compressive potential

$$\psi^{t} = \xi \psi^{t}_{c}\left(\varepsilon^{t}_{e}\right) + (1-\xi)\psi^{t}_{t}\left(\varepsilon^{t}_{e}\right), \tag{7}$$

where $\xi \in [0,1]$ is a weight function and ε^{t}_{e} is an "equivalent" transformation strain. The potentials ψ^{t}_{c} and ψ^{t}_{t} are calibrated to the measured uniaxial compression and tension stress-transformation strain responses. Jiang et al. (2016a) introduced the following definition of the equivalent strain

$$\varepsilon^{t}_{e} = J^{'}_{2} f\left(J^{'}_{r}\right), \quad J^{'}_{r} = J^{'}_{3}/J^{'}_{2}, \tag{8a}$$

where $f(J^{'}_{r})$ is a scale function and

$$J^{'}_{2} = \left(2e^{t}_{ij}e^{t}_{ij}/3\right)^{1/2}, J^{'}_{3} = \left(4e^{t}_{ij}e^{t}_{jk}e^{t}_{ki}/3\right)^{1/3}, \quad \text{and} \quad e^{t}_{ij} = \varepsilon^{t}_{ij} - \varepsilon^{t}_{kk}\delta_{ij}/3. \tag{8b}$$

In the interest of maintaining the simplicity of the modeling framework described thus far introduced by the kinematic hardening adopted for the back stress, anisotropy is introduced to the model by an affine mapping of the strains as follows (similar to approach adopted in Sedlak et al. (2012) to introduce anisotropy in shear):

$$\tilde{e}^{t} = \mathbf{D}_{1}e^{t}, \quad \hat{e}^{t} = \mathbf{D}_{2}e^{t}. \tag{9}$$

The invariants of the transformed strains then become:

$$\tilde{J}^{\prime}_{2} = (2\tilde{e}^{t}_{ij}\tilde{e}^{t}_{ij}/3)^{1/2}, \quad \tilde{J}^{\prime}_{3} = (4\tilde{e}^{t}_{ij}\hat{e}^{t}_{jk}\tilde{e}^{t}_{ki}/3)^{1/3} \tag{10a}$$

and the equivalent transformation strain

$$\tilde{\varepsilon}^{t}_{e} = \tilde{J}^{\prime}_{2} f(\tilde{J}^{\prime}_{r}), \quad \tilde{J}^{\prime}_{r} = \tilde{J}^{\prime}_{3}/J^{\prime}_{2}. \tag{10b}$$

The scale function f is chosen as follows:

$$f(\tilde{J}^{'}_{r}) = \cos\left\{\cos^{-1}\left[1 - a\left(\tilde{J}^{'3}_{r} + 1\right)\right]/c\right\}, \tag{11}$$

with parameters a and c and $f^{'}(0) = f''(0) = f^{iv}(0) = f^{v}(0) = 0$ to ensure finite moduli as $\tilde{J}^{'}_{r} \to 0$ (see Landis, 2003). Here $\tilde{J}^{'}_{r} = 1$ represents uniaxial extension and $\tilde{J}^{'}_{r} = -1$ uniaxial contraction.

The weight function ξ is selected to be a function of $\tilde{J}^{'}_{r}$ as follows:

Table 1
Model parameters for axial tensile and compressive responses.

Model	E GPa	ν	σ_o MPa	b	h_0 GPa	h_1 GPa	h_2 GPa	ε_1 (%)	ε_2 (%)
Tens.	66.3	0.425	110.3	2500	2137	−11.4	1534	3.0	3.4
Comp.	66.3	0.425	110.3	2500	1534	2.78	1534	3.0	3.4

$$\xi = \frac{f(\widetilde{J}'_r) - f(1)}{f(-1) - f(1)}, \tag{12}$$

thus facilitating the generalization of (7) to multiaxial states. Therefore, for $\xi(1) = 0$ (7) reduces to uniaxial tension and for $\xi(-1) = 1$ to uniaxial compression.

The form of the mappings D_i chosen expressed in Voigt notation is as follows:

$$\mathbf{D}_i = \begin{bmatrix} \mathbf{A}_i & \mathbf{0} \\ \mathbf{0} & \mathbf{I} \end{bmatrix}, \quad \text{where} \quad \mathbf{A}_i = \begin{bmatrix} 1 & 0 & 0 \\ 0 & A_i & 1-A_i \\ 0 & 1-A_i & A_i \end{bmatrix}, \; i = 1, 2. \tag{13}$$

This single parameter mapping ensures that e^t_{11} remains unchanged, imposes transverse anisotropy and incompressibility, and the shear strains remain unchanged. Added flexibility is provided by mapping the two invariants with different parameters: A_1 for $\widetilde{J}_2$ and A_2 for $\widehat{J}'_3$. The role of the two parameters and the procedure for selecting them is outlined in Appendix B.

The back stress is then written as:

$$\sigma^B_{ij} = \xi \frac{d\psi^t_c}{d\widetilde{\varepsilon}^t_e} \frac{\partial \widetilde{\varepsilon}^t_e}{\partial \varepsilon^t_{ij}} + (1-\xi) \frac{d\psi^t_t}{d\widetilde{\varepsilon}^t_e} \frac{\partial \widetilde{\varepsilon}^t_e}{\partial \varepsilon^t_{ij}} + \xi' \left(\psi^t_c - \psi^t_t\right) \frac{\partial \widetilde{J}_r}{\partial \varepsilon^t_{ij}}, \tag{14}$$

where $\xi' \equiv \frac{\partial \xi}{\partial \widetilde{J}_r}$.

Reduction to uniaxial stress state in the axial direction using the derivatives in Appendix A results in:

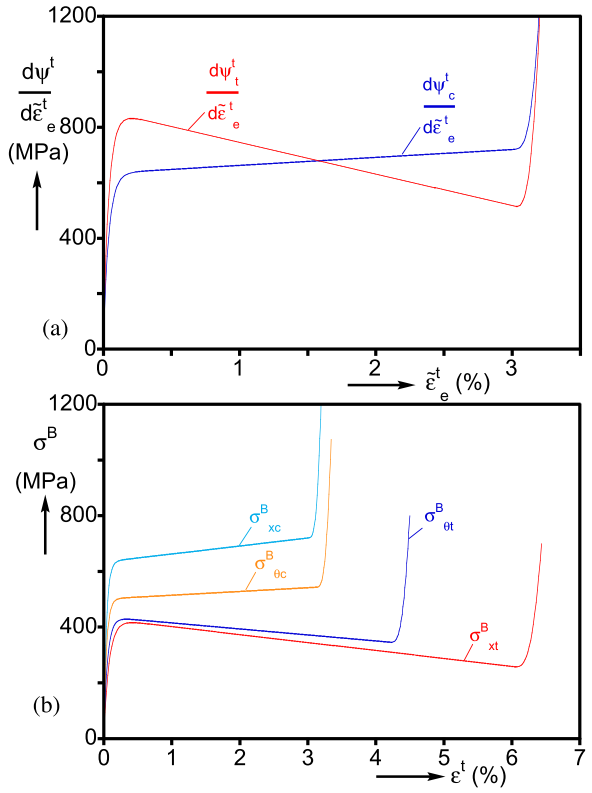

Fig. 7. (a) Adopted potential functions for axial tension and compression. (b) Associated back stress for compression and tension in hoop and axial directions.

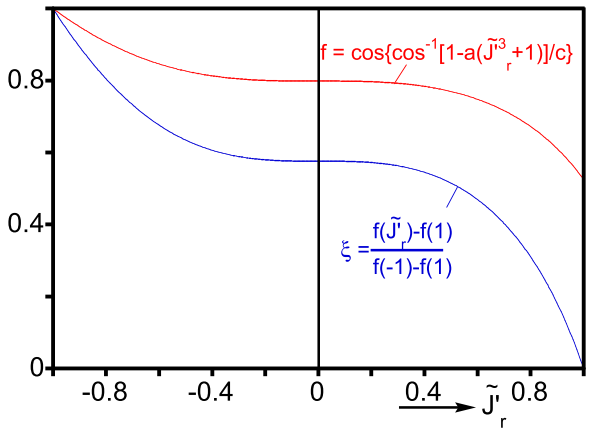

Fig. 8. Scale function $f(\widetilde{J}_r^{'})$ that interpolate tension/compression asymmetry and weight function $\xi(\widetilde{J}_r^{'})$ that generalizes it to arbitrary strain states.

$$\sigma_{11t} - f(1)\frac{d\psi_t^t}{d\widetilde{\varepsilon}_e^t} = \sigma_o, \text{ and } |\sigma_{11c}| - f(-1)\frac{d\psi_c^t}{d\widetilde{\varepsilon}_e^t} = \sigma_o. \tag{15}$$

The uniaxial back stresses in the other two directions are influenced by scaling and anisotropy and they become

$$\sigma_{22t}^B = \sigma_{33t}^B = \left[\xi(\beta)\frac{d\psi_c^t}{d\widetilde{\varepsilon}_e^t} + (1-\xi(\beta))\frac{d\psi_t^t}{d\widetilde{\varepsilon}_e^t}\right]\ \gamma f(\beta)\ , \tag{16a}$$

$$|\sigma_{22c}^B| = |\sigma_{33c}^B| = \left[\xi(-\beta)\frac{d\psi_c^t}{d\widetilde{\varepsilon}_e^t} + (1-\xi(-\beta))\frac{d\psi_t^t}{d\widetilde{\varepsilon}_e^t}\right]\gamma f(-\beta)\,, \tag{16b}$$

where $\beta = [(9A_2^2 - 9A_2 + 2)/2]^{1/3}$ and $\gamma = [3A_1^2 - 3A_1 + 1]^{1/2}$.

3.1.1. Calibration

The back stress potentials ψ_c^t and ψ_t^t are each calibrated for best fitting of the compressive and tensile stress-average strain responses of the material at 23 °C in Fig. 2b using the following expression (similar to (B1) in Jiang et al. (2016b)):

$$\frac{d\psi_{ct}^t}{d\varepsilon_e^t} = h_0\widetilde{\varepsilon}_e^t + (h_1 - h_0)\left[\widetilde{\varepsilon}_e^t - \frac{1}{b}\left(1 - e^{-b\widetilde{\varepsilon}_e^t}\right)\right]$$
$$+(h_2 - h_1)(\varepsilon_2 - \varepsilon_1)\begin{cases} 0 & \widetilde{\varepsilon}_e^t \le \varepsilon_1 \\ \left(2.5\zeta^4 - 3\zeta^5 + \zeta^6\right) & \varepsilon_1 \le \widetilde{\varepsilon}_e^t \le \varepsilon_2 \\ 0.5 + \zeta & \varepsilon_2 \le \widetilde{\varepsilon}_e^t \end{cases}, \tag{17}$$

where $\zeta = (\widetilde{\varepsilon}_e^t - \varepsilon_2)/(\varepsilon_2 - \varepsilon_1)$. The fitting parameters $\{b,\ h_0,\ h_1,\ h_2,\ \varepsilon_1,\ \varepsilon_2\}$ listed in Table 1 give the positive slope to the compressive derivative, the softening branch for the tensile derivative, as well as the saturation with which the transformation terminates as shown in Fig. 7a.

The constants a and c in the scale function $f(\widetilde{J}_r^{'})$ in (11) are assigned the values 0.736 and 2.026 respectively, which produces $f(0) = 0.8$ and $f(1) = 0.525$ along with the defined$f(-1) = 1$, resulting in the shape shown in Fig. 8– these values determine the scaling of the asymmetry. The uniaxial compression and tension back stresses in the axial and hoop directions are plotted in Fig. 7b. The tension-compression asymmetry is reflected first in the up-down-up nature of the axial tensile response and the monotonically increasing modulus of the compressive one; and second by the transformation strain in the compressive response being about one half the value of tensile one while the stress being nearly double. Anisotropy is responsible for the back stress differences between the axial and hoop directions. $\sigma_{\theta t}^B$ retains the partially softening character of σ_{xt}^B but with a significantly reduced strain extent and a somewhat higher stress level. Furthermore, $\sigma_{\theta c}^B$ retains the hardening character of σ_{xc}^B but with a reduced stress level and slightly larger strain extent.

The resultant axial and hoop tensile stress-strain responses are compared to the measured ones in Fig. 9a. The calibration responses exhibit the up-down-up nature of the corresponding back stresses for both directions. The initial moduli follow the experimental ones quite closely. The upper negative slopes are placed at stress levels so that the corresponding Maxwell stresses match the stress plateaus traced in the experiments (see Hallai and Kyriakides, 2013). The extent of the transformation strain in the axial direction agrees well with the measured response. The anisotropy parameters $\{A_1, A_2\}$ are selected for acceptable fit of several of the biaxial responses (see Appendix B), and this results in some over-prediction of the strain extent in the hoop direction. Since the elastic modulus of the two

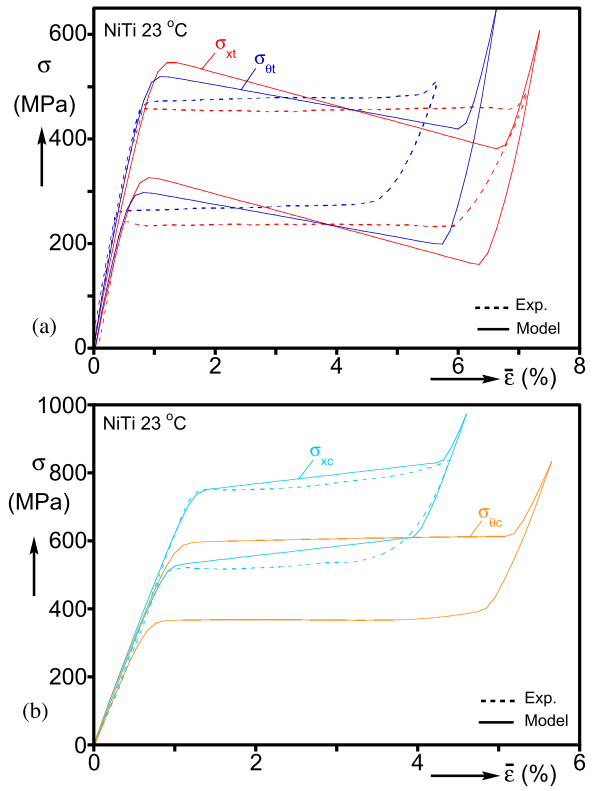

Fig. 9. (a) Comparison of calibrated tensile axial and hoop stress–strain responses – characterized by partial softening – to the measured responses. (b) Comparison of calibrated compressive axial and hoop stress-strain responses – characterized by monotonic hardening – to the measured axial response.

phases is assumed to be the same, the initial unloading modulus is stiffer than those of the two experiments. Furthermore, the nonlinear part of unloading is fitted to compression, which is stiffer. The softening slopes are the same for the upper and lower plateaus, and the size of the transformation surface is not affected by anisotropy. Consequently, the lower Maxwell stress plateau matches well that of the measured σ_{xt} and is lower than the one measured for $\sigma_{\theta t}$.

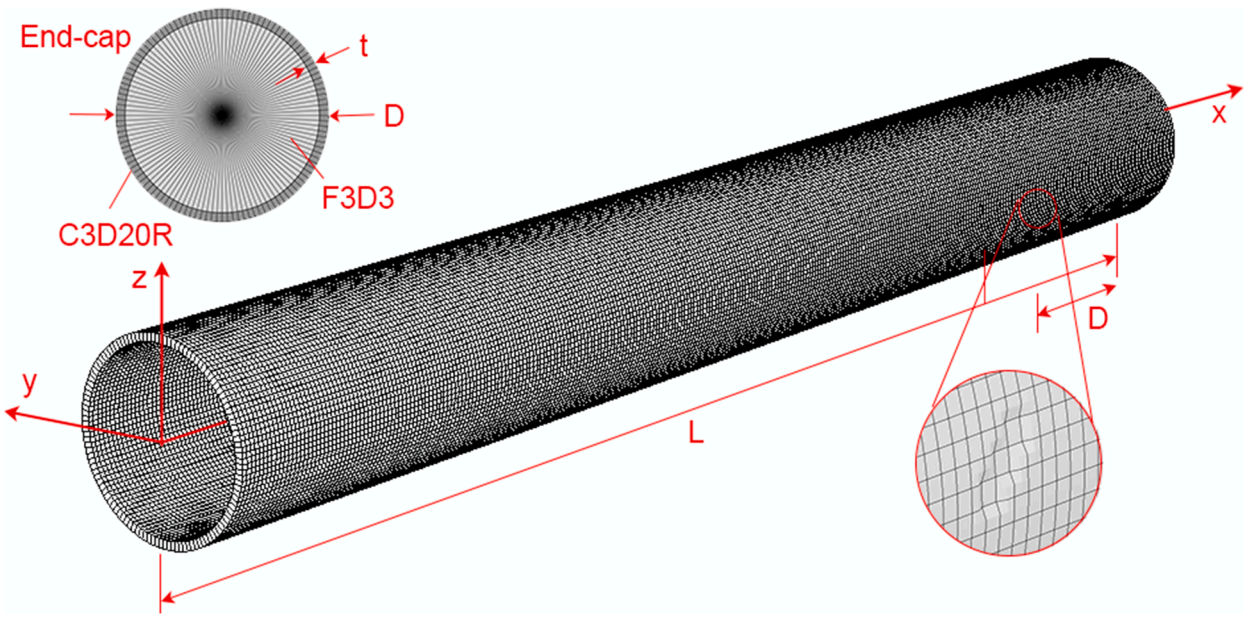

Fig. 10. Geometry and finite element mesh of the model tube and fluid cavity.

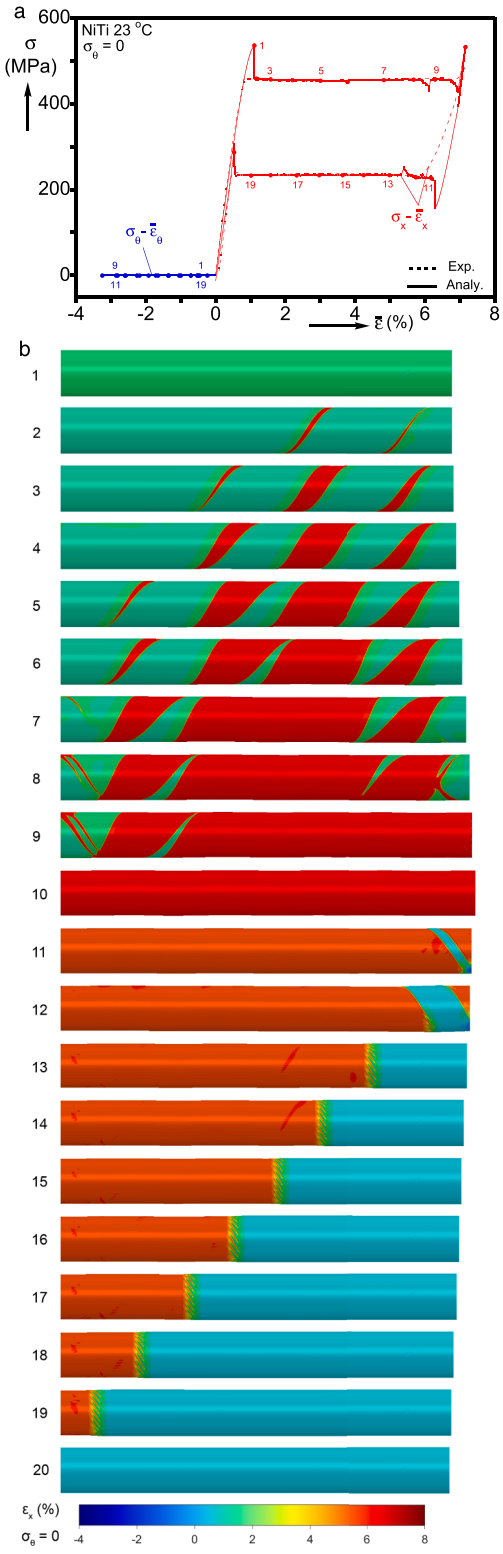

Fig. 11. (a) Calculated and measured stress-average strain responses for the uniaxial tension ($\alpha = \infty$). (b) Sequence of calculated axial strain contours ($x - z$ plane) corresponding to the numbered bullets marked on the responses in (a).

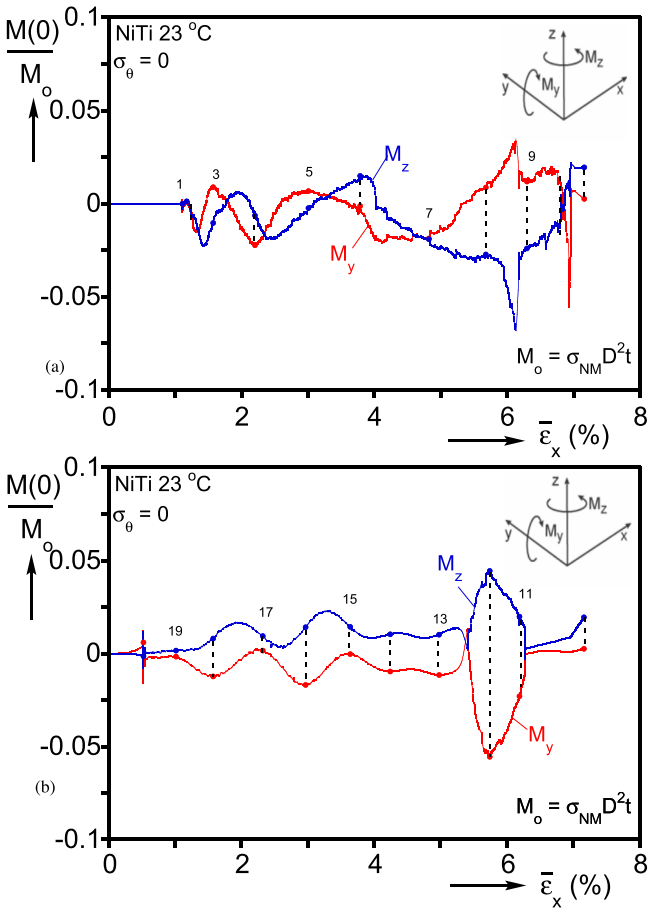

Fig. 12. Moments M_y and M_z induced by the inhomogeneous deformation vs. the average axial strain in the uniaxial tension case during: (a) loading, and (b) unloading.

The compressive responses predicted by the model for the two directions are plotted in Fig. 9b. Included is the measured axial compressive response. The hardening nature and smaller transformation strain of σ_{xc} are reproduced well, while the stress level of the unloading branch is somewhat higher because the size of the transformation stress σ_o is assumed to have the same value as the tensile response. The anisotropy adopted predicts lower transformation stress and increased transformation strain for the hoop compressive response. Further improvement of this prediction requires compressive experimental data in the transverse direction that are challenging to obtain.

3.2. Finite element model

The biaxial loading of NiTi tubes is analyzed numerically using a finite element model developed in ABAQUS. A tube of length L, diameter D, and wall thickness t, is meshed using second-order reduced integration solid elements, C3D20R. The model tube dimensions match those of the test section of the experiments in Bechle and Kyriakides (2016a): $\{50 \times 6.33 \times 0.273\}$ mm (Fig. 10). The results that follow are generated using elements with nearly square inner and outer surfaces, with one element through the thickness, 120 around the circumference and 314 along the length. This mesh is chosen following convergence studies for good reproduction of the finer features of the localization patterns observed in the experiments. The convergence studies also demonstrated that, as in our previous works (Jiang et al., 2017b, 2017c; Hallai and Kyriakides, 2011) the mesh density does not influence the overall structural response or the patterns significantly, including the number of prongs. Its main effect is limited to controlling the width of the transition zone separating transformed and untransformed domains. For alternative schemes of handling unstable material behavior using nonlocal/higher order gradient methods, see for example Frost et al. (2021); Rezaee-Hajidehi and Stupkiewicz (2021). However, such methods come with increased computational costs.

The model is pressurized internally using a cavity formed by incompressible fluid elements F3D3 and F3D4. The F3D4 surface elements have the same axial and circumferential distribution as the inner surface of the tube and connect to the four corners of each solid element. The tube ends are capped by additional F3D3 surface elements as shown in Fig. 10.

In the experiments thick steel tubular inserts were placed inside each end and the outside was clamped using an axisymmetric

Table 2
Geometric parameters and main results from biaxial analyses performed on NiTi tubes.

No.	α	D mm	t mm	L mm	ϕ°	σ_{xNM} MPa	$\sigma_{\theta NM}$ MPa	σ_{xNA} MPa	$\sigma_{\theta NA}$ MPa	$\Delta\varepsilon^t_{xM}$ %	$\Delta\varepsilon^t_{\theta M}$ %	W^t MPa
1	−1	6.319	0.273	31.25	40	−324	324	−159	159	−2.63	5.34	12.8
2	−0.75	6.319	0.273	31.25	39	−272	363	−143	191	−2.64	5.33	12.9
3	−0.5	6.324	0.272	37.5	38	−196	392	−101.5	203	−2.52	5.42	12.8
4	−0.375	6.324	0.272	37.5	37	−157	418	−82	218	−2.45	5.46	13.0
5	−0.2	6.323	0.272	37.5	35.4	−87	438.5	−46	230	−2.23	5.53	12.5
6	0	6.323	0.272	50	34.3	0	478	0	254	−2.08	5.63	13.2
7	0.2	6.323	0.272	50	32	104	521	56	279	−1.98	5.37	15.0
8	0.375	6.323	0.271	50	28	214.5	572	114	305	−1.87	5.29	16.9
9	0.5	6.318	0.272	50	21	296	591.5	162.5	325	−1.37	4.62	14.6
10	0.6	6.319	0.272	50	0	362	603	201	335	−0.82	4.21	12.9
11	0.85	6.322	0.281	50	0	540	635	325.5	383	0.02	3.68	10.4
12	0.9	6.322	0.281	50	0	567	630	342	380	0.30	3.36	9.60
13	1	6.319	0.277	50	(90)	620	620	413	413	0.98	2.79	9.30
14	1.2	6.319	0.267	50	(90)	667	556	436	363	1.91	2.09	12.8
15	1.3	6.319	0.267	50	90	682	524.5	395	304	4.84	−1.29	15.9
16	1.5	6.319	0.267	50	63	679.5	453	390	260	5.18	−1.45	19.9
17	1.8	6.319	0.267	50	61	637	354	329	183	5.62	−2.12	22.6
18	2	6.323	0.271	50	60	626	313	321	160.5	6.22	−2.33	23.9
19	3	6.323	0.275	50	58	194.5	579	306	102	6.32	−2.60	21.2
20	4	6.323	0.275	50	57.6	546	136.5	281	70	6.35	−2.73	18.9
21	8	6.323	0.271	50	57	506	63	261	32	6.45	−2.93	15.9
22	∞	6.318	0.270	50	56.2	460	0	233	0	6.14	−2.79	14.1

locking assembly. In the present model, the resultant stress concentration is avoided by allowing the ends at $x = 0$ and L to freely expand radially. Simultaneously, the average in-plane nodal displacements and rotations at the ends are prescribed to be zero (i.e., $\sum_i^n u_y = \sum_i^n u_z = \sum_i^n u_\theta = 0$). The axial degrees of freedom of all nodes at $x = 0$ are made zero while at $x = L$ are assigned either a value δ_x or a stress σ_x.

The experiments were performed under radial loadings $\sigma_x = \alpha\sigma_\theta$, with the stresses related to the axial force, F, and internal pressure, P, through Eq. (1b). Such stress states are replicated using a control loop in a UAMP. For hoop stress dominant paths, the volume of the fluid inside the cavity is incrementally prescribed. The resultant pressure is then used to calculate the required axial force increment to achieve the axial-hoop stress proportionality of the experiment. For axial stress dominant stress paths (typically for $\alpha > 1.2$), the axial displacement is prescribed incrementally instead. The induced axial force is recorded and the pressure in the cavity is adjusted to produce the required stress proportionality.

The anticipated localization is induced by a small thickness depression placed at a distance D from one of the ends. The depression extends over an area of about $2t \times t/2$, is $0.02t$ deep, and has transition zones of $t/2$ all around. Furthermore, it is oriented at 45° to the axis of the tube as shown in the zoomed detail in Fig. 10.

4. Simulation of biaxial experiments

The numerical analysis outlined is now used to simulate a number of the biaxial experiments of Bechle and Kyriakides (2016a). The two uniaxial loading cases that were used in the calibration of the constitutive model will be reviewed first and compared to the corresponding experiments. The two simulations will illustrate the main effects of the assumed dual up-down-up material response on tubular structures. They will be followed by results from representative simulations that span the stress ratios of the experiments. The results will be the basis for evaluating the model performance in reproducing the effect of biaxiality on the recorded responses and the deformation patterns.

Pure Axial Tension: $\sigma_\theta = 0$

The calculated nominal axial stress-average strain response is plotted in Fig. 11a together with the experimental one. Twenty deformed configurations of the model tube corresponding to the numbered bullets marked on the response are shown in Fig. 11b. The associated axial strain is superimposed as color contours. The experimental response was incorporated in the calibration of the up-down-up material response (Figs. 7b and 9a) and, consequently, the calculated one is in very good agreement. The two stress plateaus match closely the measured ones, and so does the extent of the upper one. Unloading (⑩ to ⑪) follows a somewhat stiffer trajectory, a consequence of fitting the unloading branch in Fig. 9a with a steeper slope. A minor difference is that the calculated response exhibits a stress peak and valley at the nucleation of M and A respectively. Such initiation stress maxima/minima are characteristic of localization instabilities, which in the experiment were masked by the stress concentrations at the clamped ends.

The M-phase nucleates from the local imperfection on the right in the form of a narrow sinistral helical band with an inclination of 56° to the axis of the tube – image ②. In the experiment the martensitic band opted for the alternate characteristic with a dextral inclination of 55.8°. In subsequent images, the band propagates toward the ends, on the way broadening, while the stress traces a nearly constant trajectory. The strain inside the band is 6.94% and outside it 1.06%, corresponding to the termination and beginning of

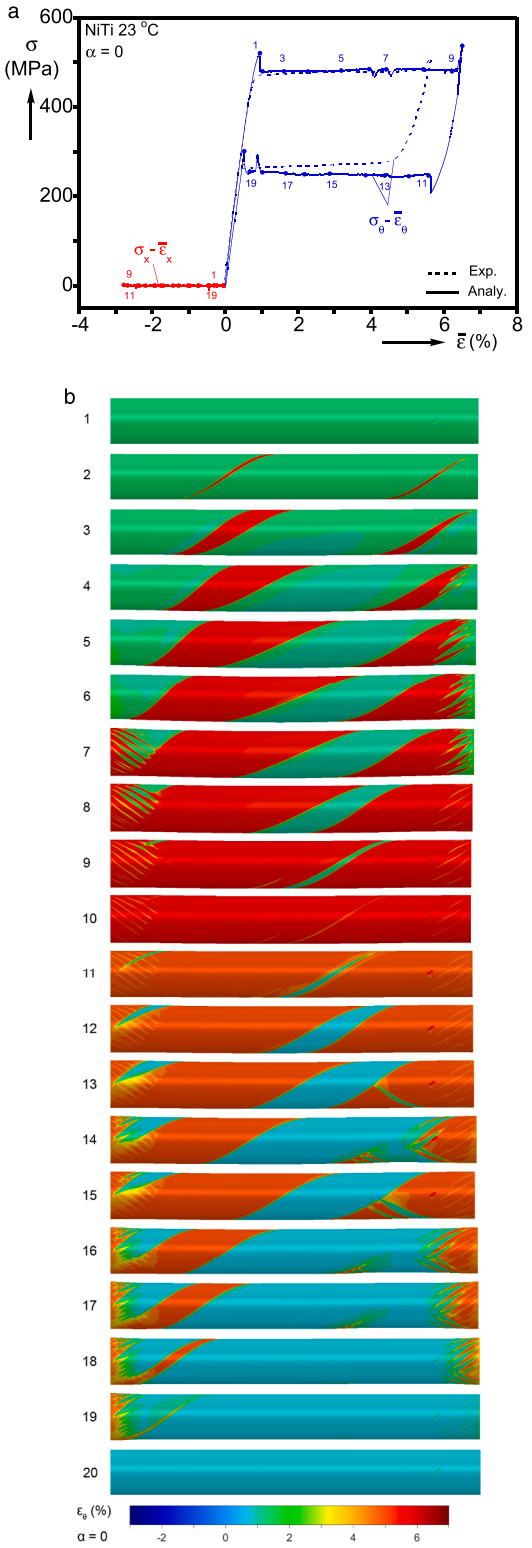

Fig. 13. (a) Calculated and measured stress-average strain responses for pure hoop stress ($\alpha = 0$). (b) Sequence of calculated axial strain contours ($x-z$ plane) corresponding to the numbered bullets marked on the responses in (a).

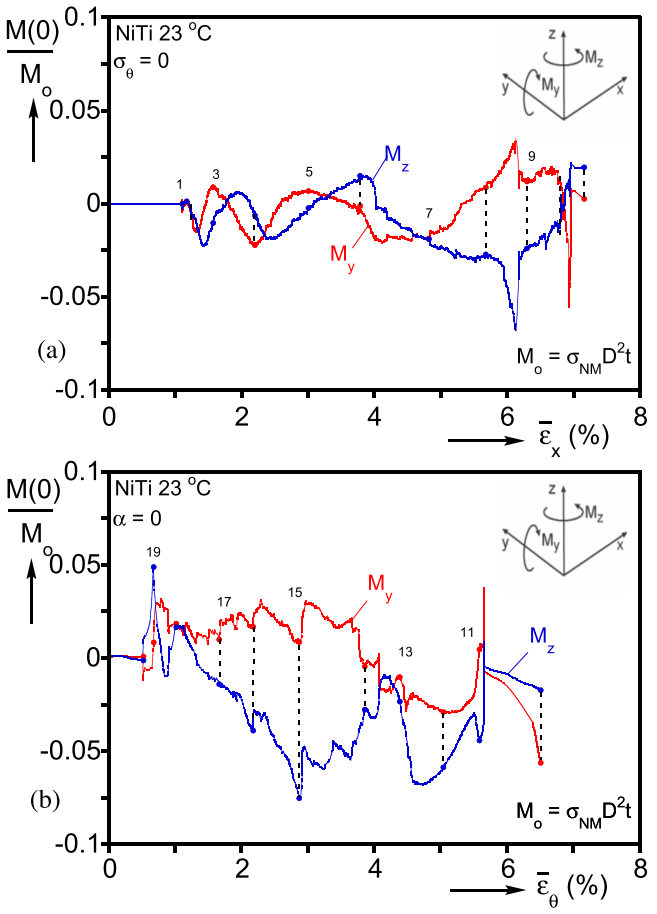

Fig. 14. Moments M_y and M_z induced by the inhomogeneous deformation vs. the average hoop strain in the pure hoop stress case during: (a) loading, and (b) unloading.

the upper plateau, respectively. The remaining islands of low strain material at the ends transform last with the right end going first followed by the one on the left. When a remaining band encounters one of the relatively unconstrained ends, it transforms in a snap fashion registering as a stress valley. As in other SMA structures studied, inhomogeneous deformations induce bending that is resisted by the imposed constraints at the ends resulting in the built up of moments. The M_y and M_z moments recorded at $x = 0$ (see Fig. 10) during loading and unloading are plotted in Fig. 12a and 12b – moment M_x is much smaller and thus not shown. The normalizing moment $M_o = \sigma_{NM} D^2 t$, where σ_{NM} is the A→M plateau stress in the pure axial tension test, and the geometric variables are those of the specific tube listed in Table 2. During loading, the evolving band causes some undulations in both moments. The moments reach their extreme values between stations ⑧ and ⑩ as the low strain islands at the two ends transform.

During unloading, the deformation remains uniform until the lower strain phase nucleates at the right end as a dextral band. The localized deformation first evolves into an inclined band. The resultant asymmetric distribution of deformation causes the built-up in moments M_y and M_z observed in Fig. 12b. As the band propagates toward the left, the amplitudes of the moments increase, and reach maximum values at station ⑫. At this time, the left end of the inclined band morphs into a dextral multi-pronged front. The more symmetric nature of such fronts has a straightening effect on the tube that relieves the moments. Subsequently, the front propagates to the left gradually returning the tube to the lower strain regime with the two moments fluctuating about lower values. A small island of higher strain on the right end transforms in a snap fashion causing the small stress peak recorded between stations ⑫ and ⑬. A second stress peak is traced just before station ⑳ when the left end unloads.

It is noteworthy that in the experiment during loading the M-phase propagated via helical bands, while on unloading the A-phase spread via multi-pronged fronts, both in agreement with the calculations. This experiment was previously simulated numerically in Jiang et al. (2017a) using an earlier version of the constitutive model. Although the calculated response was also in very good agreement with the experimental one, the evolution of deformation differed: the A→M transformation exhibited mostly multi-pronged fronts, while the reverse transformation propagated via spiral bands. The difference in the deformation patterns of the two solutions can be attributed to the following:

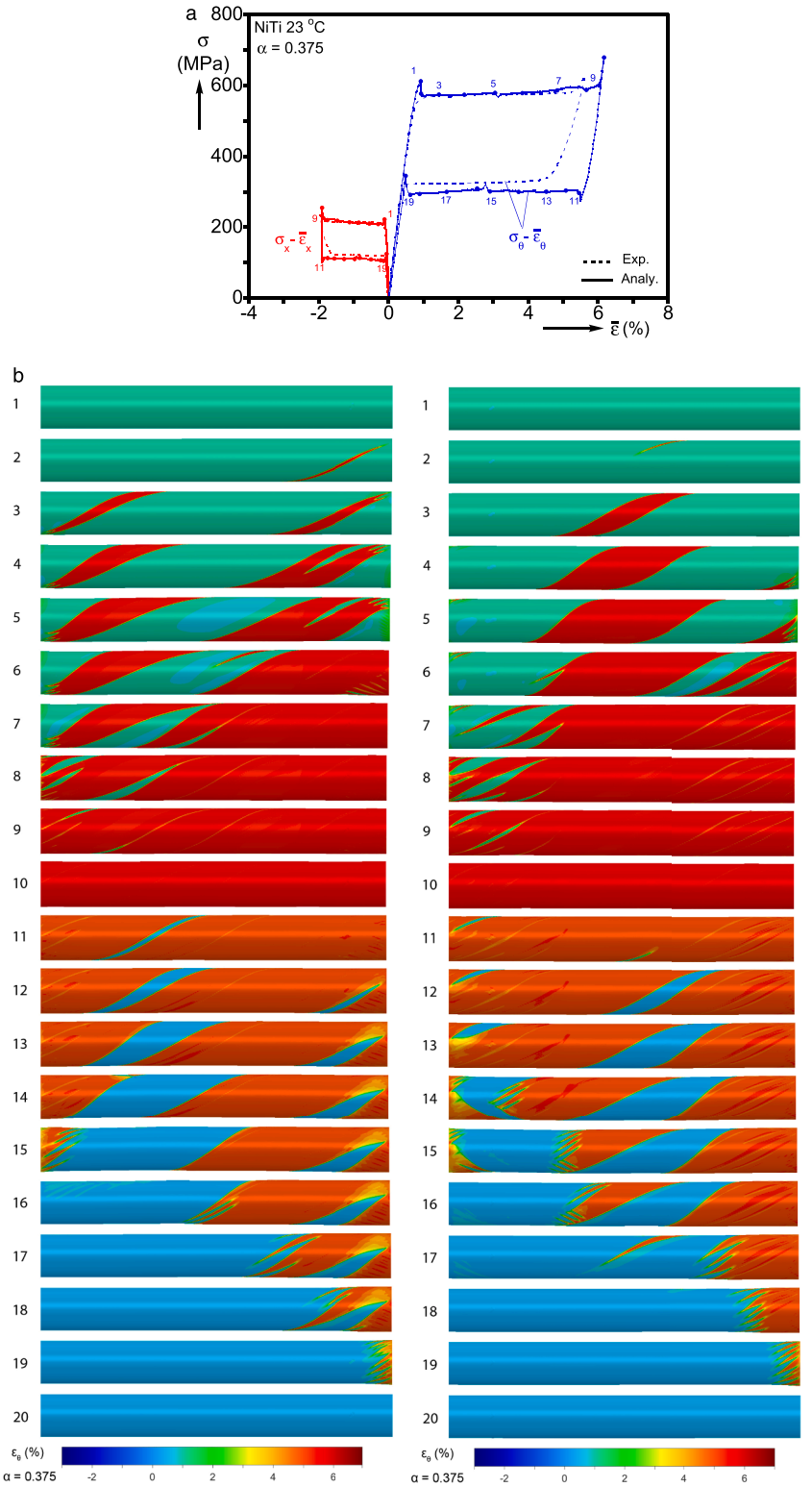

Fig. 15. (a) Calculated and measured stress-average strain responses for biaxial case $\sigma_x = 0.375\sigma_\theta$. (b) Sequences of calculated hoop strain contours corresponding to the numbered bullets marked on the responses in (a) – left front and right back views of the $x - z$ plane.

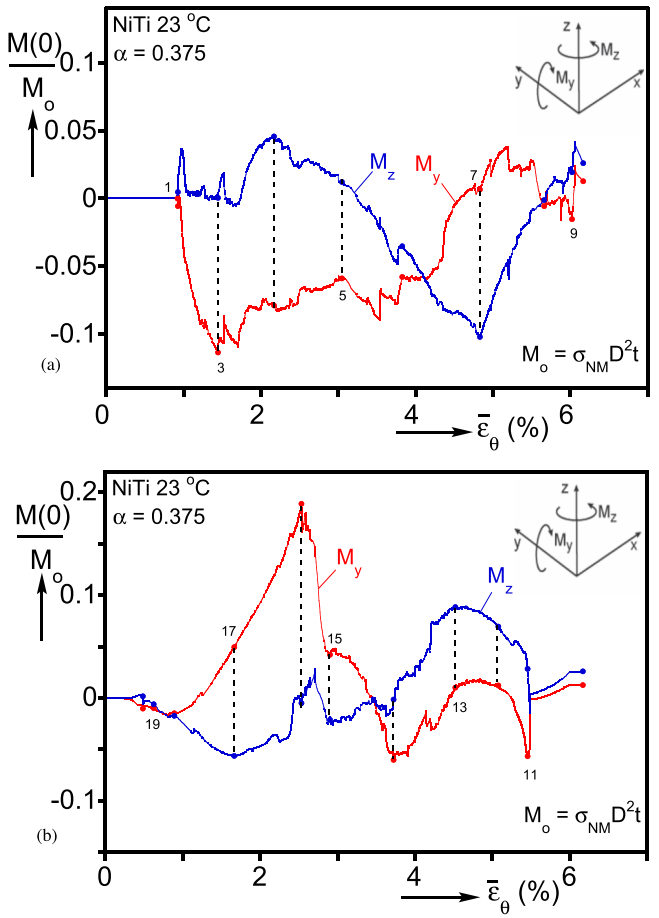

Fig. 16. Moments M_y and M_z induced by the inhomogeneous deformation vs. the average hoop strain in the biaxial case $\sigma_x = 0.375\sigma_\theta$ during: (a) loading, and (b) unloading.

a. In the present model transformation is initiated from an angled depression, whereas the previous analysis used a square depression close to one of the ends.
b. Higher slope of the M-phase in the up-down-up material response of the present model.
c. The present model applied an additional constraint at the ends, $\sum_i^n u_\theta = 0$.

These factors demonstrate that the evolution of localized deformation is sensitive to the way the band is initiated, the softening/hardening features of the assumed stress-strain response, and the imposed boundary conditions (see also Section 5 of Jiang et al., 2017a).

Uniaxial Hoop Tension: $\alpha = 0$

The calculated nominal hoop stress-average strain response is compared to the experimental one in Fig. 13a. Twenty deformed configurations with color contours of hoop strain superimposed appear in Fig. 13b, and the two moments that develop are plotted against the average hoop strain in Fig. 14. This case was part of the anisotropy calibration so the calculated response reproduces the levels of the stress plateaus quite well. The anisotropy has also reduced the difference in the strain extents. This difference will affect the rest of the biaxial responses to various degrees. Localized deformation again initiates from the thickness depression on the right in the form of a sinistral helical band. It has a helix angle of 34.3° and propagates toward the left end (image ②). The strain inside the band is 6.38%, which is smaller than the corresponding value of the axial response in Fig. 11a. In the experiment dextral bands of M-phase with a helix angle was 29° and strain of 5.5% initiated from both ends and propagated toward the center. The propagation and broadening of the band are asymmetric affecting both moments plotted in Fig. 14a. In image ⑤ the band develops a multi-pronged front that propagates toward the right end, and in image ⑦ a second one develops on the left end. Small stress valleys are registered in the response as a consequence. The transformation is completed with the multi-pronged fronts transforming the two ends causing the fluctuations in moments observed in Fig. 14b.

Unloading from station ⑩ follows a similar stiff trajectory to that in Fig. 11a. A sinistral band of lower strain representative of the A-

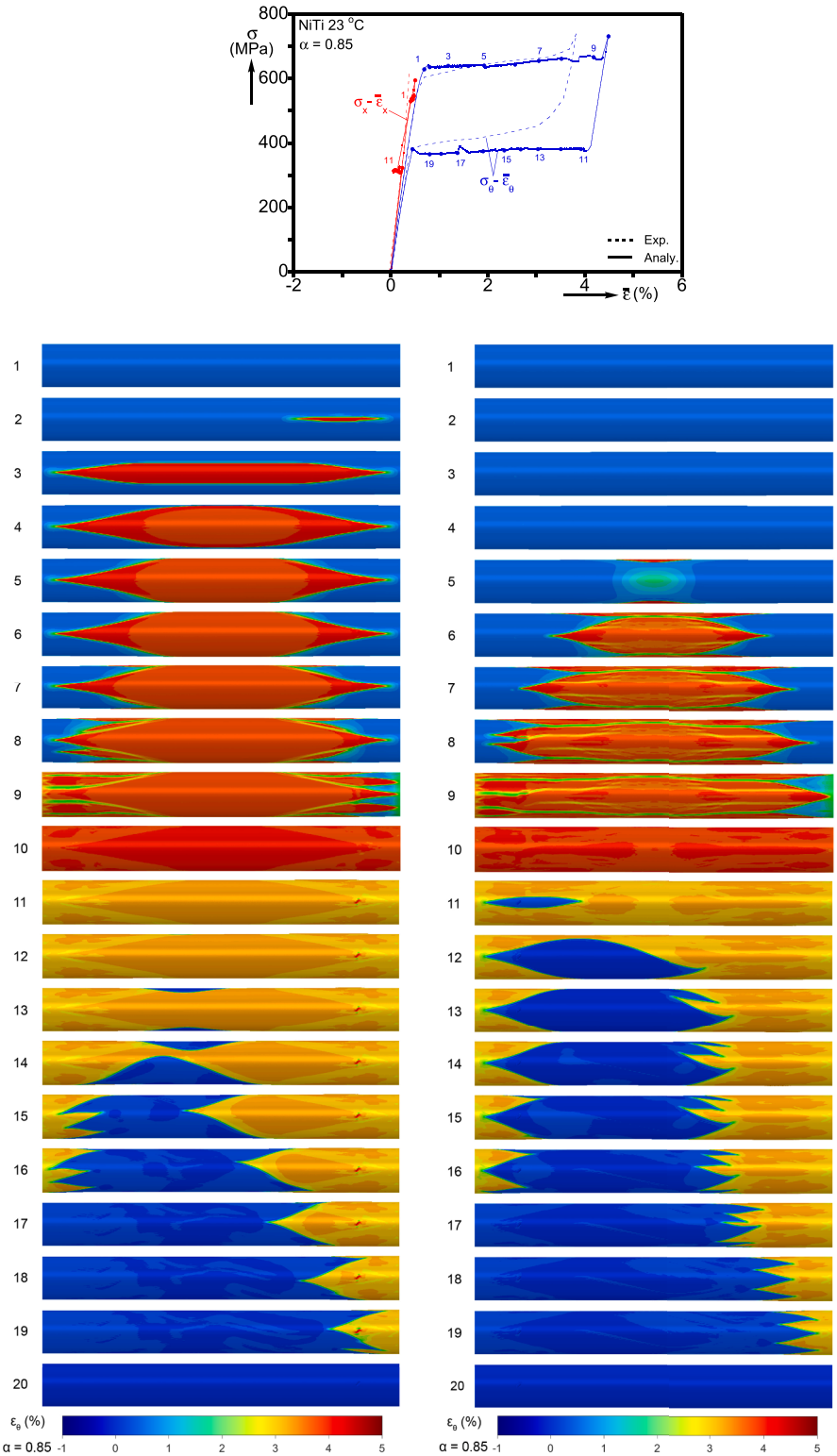

Fig. 17. (a) Calculated and measured stress-average strain responses for biaxial case $\sigma_x = 0.85\sigma_\theta$. (b) Sequences of calculated hoop strain contours corresponding to the numbered bullets marked on the responses in (a) – left front and right back views of the $x - z$ plane.

phase initiates in the middle of the tube from a site that transformed last during loading. The band propagates toward the ends and simultaneously broadens. As the fronts interact with the ends they again evolve into multi-pronged fronts. The broadening of the band in the center induces asymmetric distribution of strain responsible for the build-up and decay of the two moments in Fig. 14b. Eventually, the central band reverts to the lower strain leaving behind the two islands of higher strain at the ends as seen in images ⑯ to ⑱. The island on the right unloads first causing the stress peak just after station ⑱. The left island unloads last and is responsible for the stress peak at ⑳. Both of these events occur in a snap fashion.

$\sigma_x = 0.375\sigma_\theta$

This stress state is representative of hoop stress-dominant biaxiality ratios. The calculated nominal stress-average strain responses in the hoop and axial directions are plotted in Fig. 15a together with the corresponding experimental ones and two sets of deformed images with color contours of hoop strain superimposed are shown in Fig. 15b. For this case front and back views of the hoop strain contours are included for better visualization of the evolution of localized deformation (side with the imperfection on the left). The two moments recorded at $x = 0$ are plotted in Fig. 16a and 16b against the average hoop strain.

Biaxiality shifts the hystereses to higher stress levels with the calculated responses reproducing the experimental ones quite well. The main difference is that the A→M transformation plateau extends to 6.1%, whereas in the experiment it terminated at 5.43%. The upper stress plateaus are in nearly perfect agreement with the experiment but the unloading ones are somewhat lower.

Deformation remains uniform up to a hoop stress of 614 MPa – station ①. The stress drops sharply down to 579 MPa – station ② –, marking the nucleation of M in the form of a narrow sinistral helical band. The band initiates from the thickness depression and makes an angle of 28° to the axis of the tube. In the experiment the initial band was dextral with a larger helix angle of 32.7°. Between stations ② and ③ the band propagates to the other end of the tube broadening on the way. The band has hoop strain of 6.2%, whereas the rest of the domain is at 0.92%. The value of M_y increases reaching an extreme value at ③ when the band reaches the ends (Fig. 16a). The asymmetry in the domain starts to decrease and the magnitude of M_y is gradually reduced. Secondary branches appear on the right end, visible in images ④, causing an increase in M_z. During these events σ_θ traces a nearly constant stress plateau of 576 MPa. The band continues to broaden causing a gradual reduction in M_z and a more modest change in M_y. Soon after station ⑤, a multi-pronged band initiates on the right end that transforms the remaining lower strain zone causing small depressions in the stresses (Fig. 15a). By station ⑥, a significant part of the domain is in the higher strain regime. A secondary sinistral band has initiated whose broadening covers the remaining undeformed zone on the right (image ⑦). In the process M_y diminishes, while M_z drops to its lowest a negative value. The band front develops several sinistral prongs that propagate toward the left end. These have a straightening effect on the tube causing both moments to reduce to nearly zero by station ⑧. When the prongs reach the left end at ⑧, new small stress depressions develop. Between stations ⑧ and ⑨ the remaining small islands of low strain require a small increase in stress to transform due to incompatibility. Beyond this point, the whole domain is in the high strain regime, the stress increases sharply, and the moments decay to nearly zero. The Poisson effect dominates the axial strain keeping it negative, with the same deformation patterns as those of the hoop strain.

The unloading branches are again somewhat steeper than in the experiment. Deformation remains uniform down to a hoop stress of 273 MPa, when the A-phase nucleates once more in as a helical band at the site that transformed last to M near the middle of the domain. The strain inside the band is about 0.62% and 5.5% outside it. The resultant asymmetry causes jumps in both moments plotted in Fig. 16b. Between stations ⑪ and ⑫, the band propagates and broadens reaching both ends, causing M_z to increase and M_y to decrease. From station ⑫ to ⑬, the band widens with M_z reaching a maximum,M_y hovering close to zero, while the hoop stress traces a plateau at just over 300 MPa. As station ⑭ is approached, the band continues to broaden, but its left end starts developing a multi-pronged front apparent on the right column. The front has a straightening effect on the tube and is responsible for the gradual drop in M_z. By image ⑮, a dextral multi-pronged front has developed also and both are propagating outward. M_y is now increasing into positive territory, while M_z remains low. Moving toward station ⑯, most action takes place near the left end where the remaining island of high strain is consumed by the multi-pronged band. This event occurs in a snap fashion and is responsible for the small stress peak traced in the response in Fig. 15a. It has also resulted in a significant increase in M_y because of the asymmetric distribution of the two strain regimes in the right half of the tube. Transformation between ⑯ and ⑰ is mainly via a right propagating multi-pronged front. As more of the tube returns to the lower strain, M_y decreases. As the front approaches the right end, it becomes more symmetric causing the two moments to drop close to zero by stations ⑱ and ⑲. Once more, the last zone of high strain transforms in a snap fashion causing small spikes in stresses between stations ⑲ and ⑳. The whole domain is now in the low strain regime and further unloading of the A-phase returns the structure to zero stresses and strains.

A more detailed presentation of the evolution of localization is provided by the video: Video mmc2.

$\sigma_x = 0.85\sigma_\theta$

As the biaxiality ratio α increases, the two hystereses move to higher stress levels and reduce their strain extents. At some point the axial strain overtakes the Poisson effect entering positive territory (see Fig. 25 of Bechle and Kyriakides, 2016a). The axial strain recorded in the experiment for $\alpha = 0.85$ was close to zero, and as seen in Fig. 17a this is reproduced by the analysis. The calculated hoop stress increases with the A→M transformation stress reaching 636 MPa, which is close to the experimental value. The hoop strain extent is reduced to 4.4%, which is somewhat larger than that of the experiment. The initiation peak and valley are now both very small. The stress exhibits less hardening than in the experiment, and the lower transformation trajectory is underpredicted.

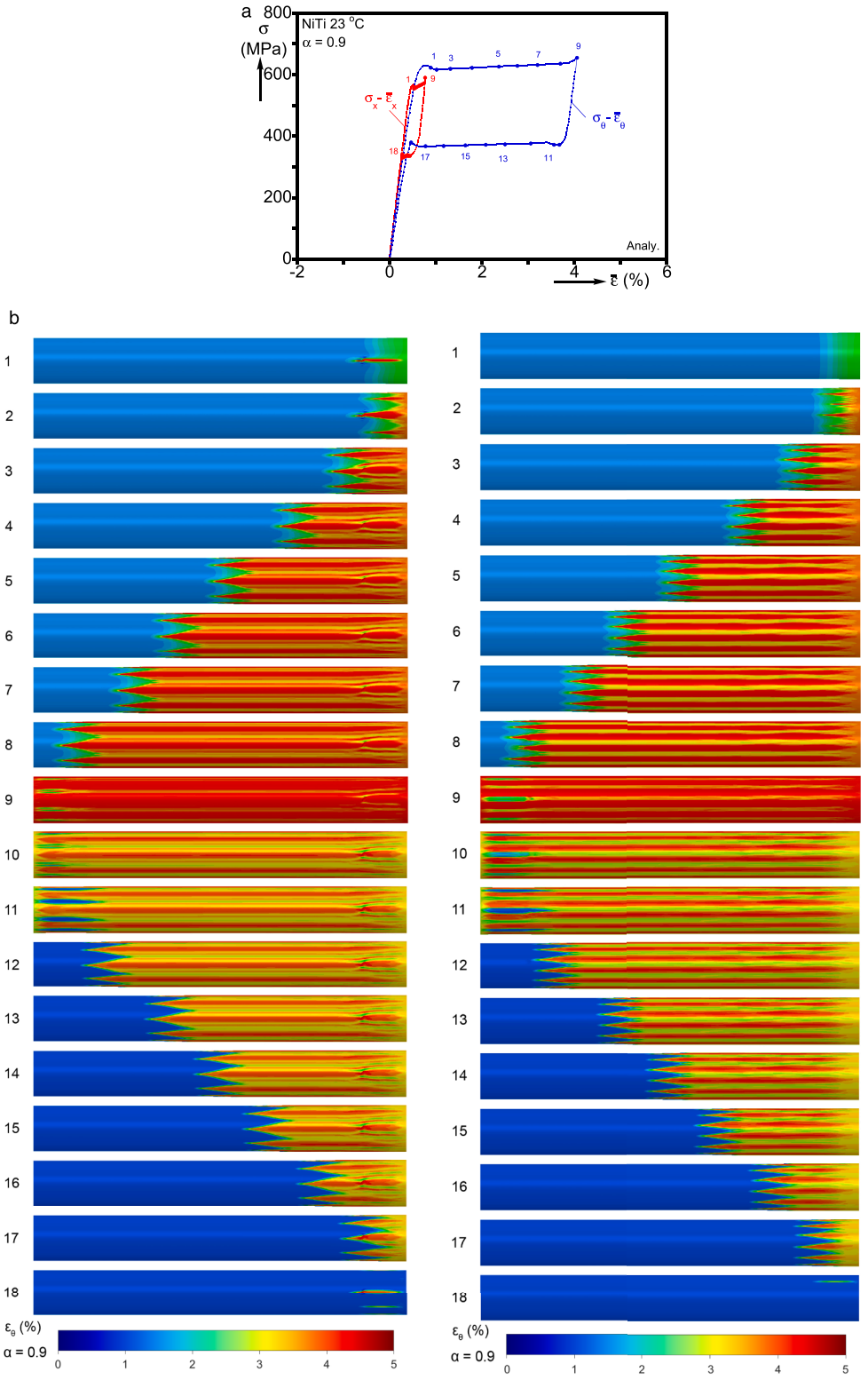

Fig. 18. (a) Calculated and measured stress-average strain responses for biaxial case $\sigma_x = 0.9\sigma_\theta$. (b) Sequences of calculated hoop strain contours corresponding to the numbered bullets marked on the responses in (a) – left front and right back views of the $x - z$ plane.

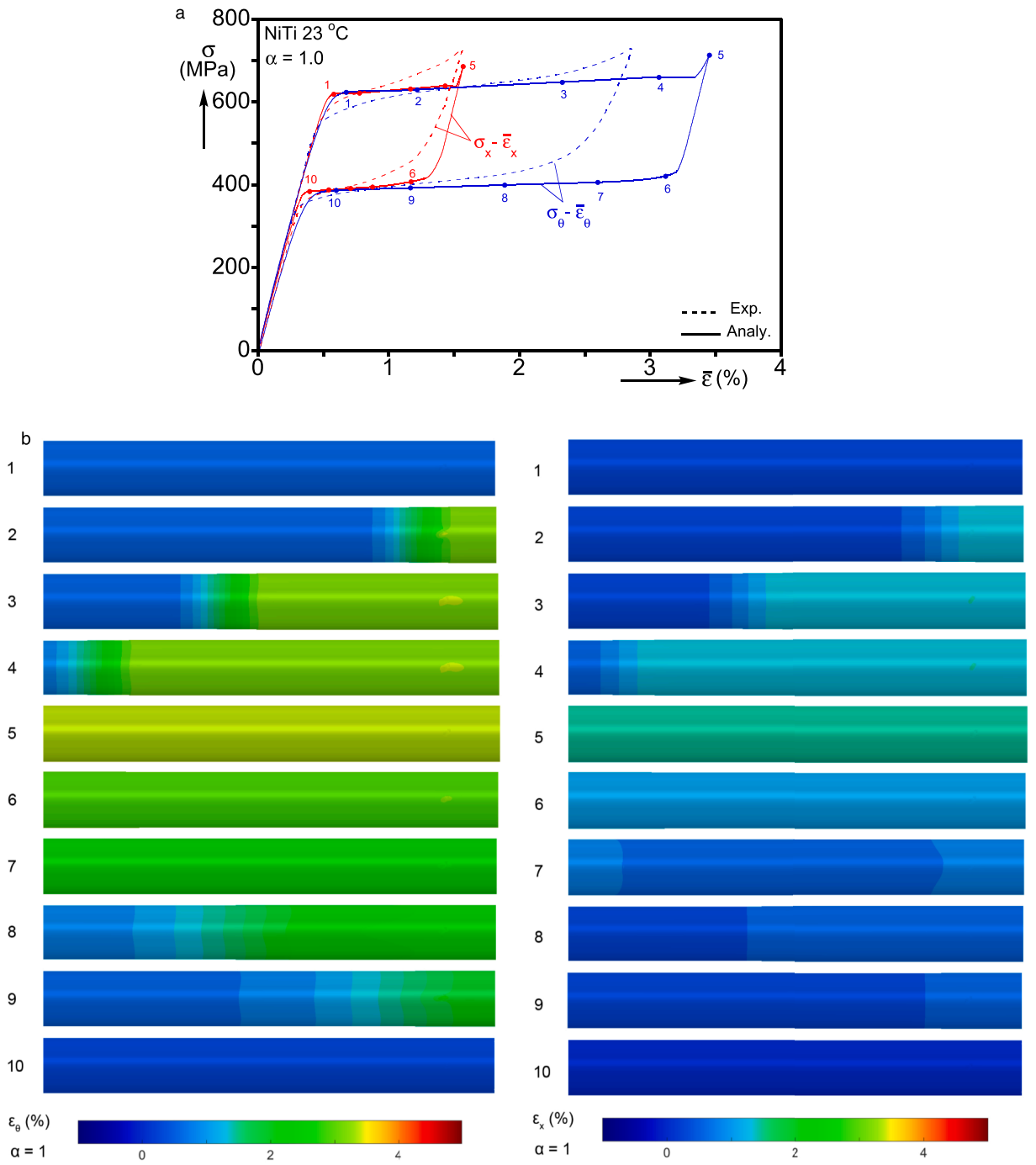

Fig. 19. (a) Calculated and measured stress-average strain responses for biaxial case $\sigma_x = 1.0\sigma_\theta$. (b) Sequences of calculated strain contours corresponding to the numbered bullets marked on the responses in (a) – left hoop and right axial strains viewed in the $x - z$ plane.

Front and back views of 20 deformed configurations are shown in Fig. 17b. Strain of about 4.4% nucleates from the imperfection in a needle-like form aligned with the axis of the tube (image ②). The band elongates and widens maintaining its sharp ends (③ and ④) while the rest of the tube remains at 0.72% strain. The moments M_y and M_z are an order of magnitude smaller than those produced by the spiral patterns in the previous cases and are not included (see Chapter 4 in Kazinakis, 2022). By station ④ the width of the axially symmetric higher deformation zone covers nearly one-half of the circumference in the central part of the tube. The one-sided deformation is no longer sustainable and a second longitudinal pattern initiates diametrically opposite the first (image ⑤), causing a small drop in stress at station ⑤. The new island of higher deformation on the back has a straightening effect on the tube. In images ⑥

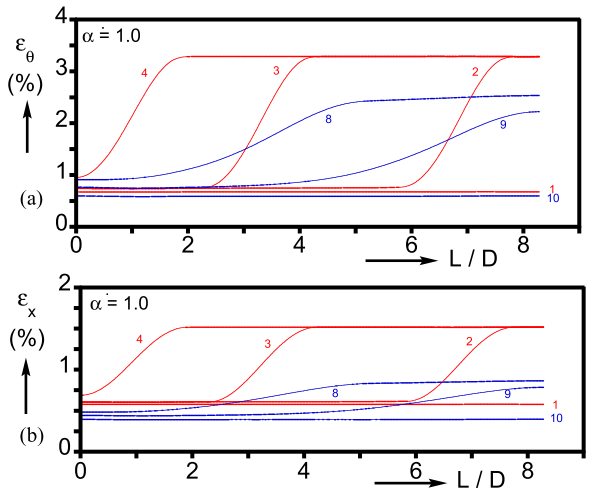

Fig. 20. Strain profiles along the length of the tube from selected configurations for biaxial case $\sigma_x = 1.0\sigma_\theta$: (a) hoop and (b) axial strains – correspond to numbered bullets in Fig. 19.

and ⑦ deformation is concentrated in the longitudinal pattern on the back causing it to broaden. By station ⑦, higher strain has covered most of the tube with the two longitudinal patterns coalescing in the central part of the tube, while the ends remain relatively undeformed. The ends are engaged by pointed longitudinal prongs that emerge from the edges of the transformed zones in the center. They appear first in images ⑧ and multiply in image ⑨ forming pointed crown-like shapes at both ends. The ends transform between stations ⑧ and ⑩ causing small stress depressions.

Unloading traces again a trajectory with a sharper knee than in the experiment. Reverse transformation initiates again as a longitudinal needle-like pattern in the back seen in image ⑪. The pattern widens and lengthens, but simultaneously its right front develops a shallow angle helical trend that evolves asymmetrically – ⑫. In the way of straightening the tube, a second pointed finger arises on the right end (image ⑬), and a third one seen in image ⑭. Concurrently, the circumferential growth of this pattern continues so that soon after image ⑭ the lower strain regime covers the full circumference near the center of the tube. Between stations ⑭ and ⑯ most of the unloading takes place on the left end through pointed prongs seen in images ⑮ and ⑯. Just before station ⑰, the left end unloads to the lower strain in a snap fashion causing the small stress peak in Fig. 17a. Beyond this point, several new pointed prongs develop on the right forming a crown-like front through which the remaining island of higher strain is transformed. The stress peak just before station ⑲ is associated with the unloading of this island. The transformation patterns in the experiment were also oriented along the tube axis with somewhat more diffuse longitudinal fingers that are similar of those developed during the forward transformation (Fig. 16 of Bechle and Kyriakides, 2016a).

A more detailed presentation of the evolution of localization is provided by the video: Video mmc1.

$\sigma_x = 0.9\sigma_x$

With a small further increase of the stress ratio to 0.9, the axial strain becomes positive (Fig. 18a) and the deformation pattern longitudinal and striped (Fig. 18b). The hoop stress is at a similar level to that of $\alpha = 0.85$, and the induced transformation strain is reduced further to about 4%. The hystereses exhibit small initiation peaks and valleys, and transformation induces a modest increase in the slopes of both the loading and unloading branches. The hystereses of experiments at stress ratios of 0.89 and 0.92 (unpublished) had similar stress levels and strain extents but were clearly monotonic and without stress peaks and valleys. Front and back views of a set of deformed configurations are shown in Fig. 18b. A local axial band of strain aligned with the axis of the tube initiates from the imperfection (image ①). At a slightly higher average strain, additional bands nucleate progressively from the front to the back (image ②). The bands are aligned with the axis of the tube with spear-like fronts. The 11 bands of about 4% strain are separated by narrow zones of lower strain. Because the bands in the front of the domain nucleated first, they are wider than the ones of the back. In images ③ to ⑧ the pointed crown-like front propagates in a steady-state manner to the left maintaining its striped character. The axially aligned and nearly axisymmetric transformation pattern does not cause any significant built-up of moments. The left end is transformed next and the stripes of lower strain at the end (image ⑨). It is worth pointing out that in biaxial expedients of $\alpha = 0.89$ and 0.92, transformation involved higher strain axial features with pointed ends also, albeit with not so symmetric patterns.

Upon unloading to station ⑩, the lower strain stripes reappear. Interestingly, here the first local axial bands of strain of about 0.48% nucleate near the left end on the back, inside steaks of lower strain (image ⑩). At station ⑪, close to the bottom of the stress valley, similar bands appear in all lower strain stripes around the circumference. Subsequently, strain of about 0.48% spreads to the whole cross section with a crown-like front with its pointed ends inside the weaker strain stripes (image ⑫). In images ⑫ to ⑰ the front propagates in a steady-state manner toward the right with the end returning to the lower strain in nearly the reverse of loading – see one of the last slivers of higher strain at the imperfection in image ⑱.

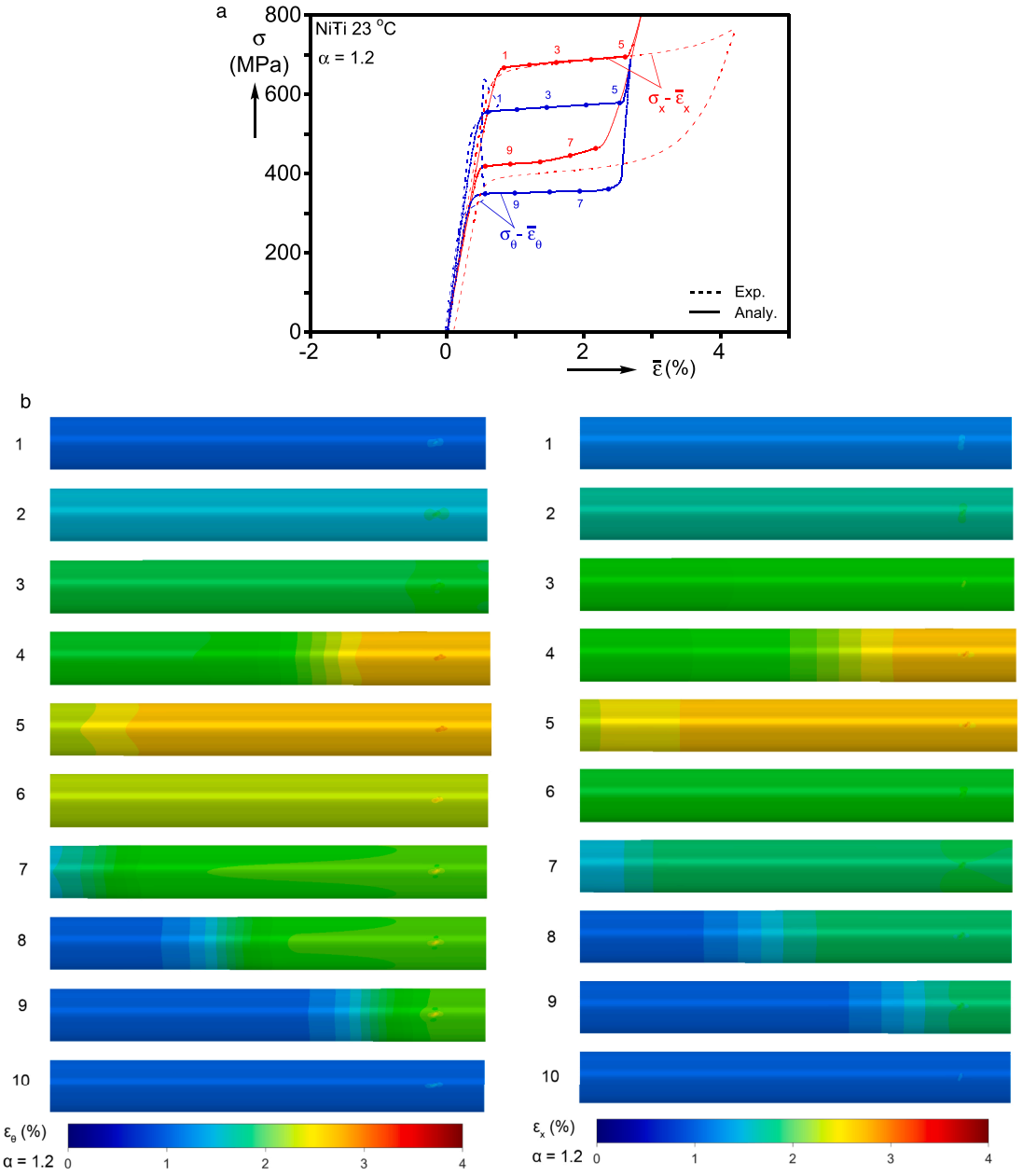

Fig. 21. (a) Calculated and measured stress-average strain responses for biaxial case $\sigma_x = 1.2\sigma_\theta$. (b) Sequences of calculated strain contours corresponding to the numbered bullets marked on the responses in (a) – left hoop and right axial strains viewed in the $x - z$ plane.

$\sigma_x = \sigma_\theta$

Fig. 19a compares the calculated and measured nominal stress-average strain responses and Fig. 19b presents ten deformed configurations with the axial and hoop strain superimposed. The hystereses develop positive strains of unequal extents as was the case in the experiment. The axial transformation strain matches the measured value, while the hoop strain is overestimated – consequence of the anisotropy adopted (Appendix B). The nucleation peaks and valleys present in other biaxiality ratios are replaced by smooth stress transitions. The transformation stress of about 625 MPa is close to the experimental value. By the completion of transformation, the stresses increase to about 660 MPa, a smaller increase than in the experiment, which exhibited significantly more hardening. Transformation nucleates on the right and leads to mild inhomogeneity featuring patterns that are orthogonal to the axis of the tube (see images ② to ④ in Fig. 19b). Furthermore, the front separating the two zones is diffuse with the strain varying over a length of about 1.5D (see profiles ② to ④ in Fig. 20). The experimental results in Fig. 4 show also very mild inhomogeneity but with longitudinal diffuse features.

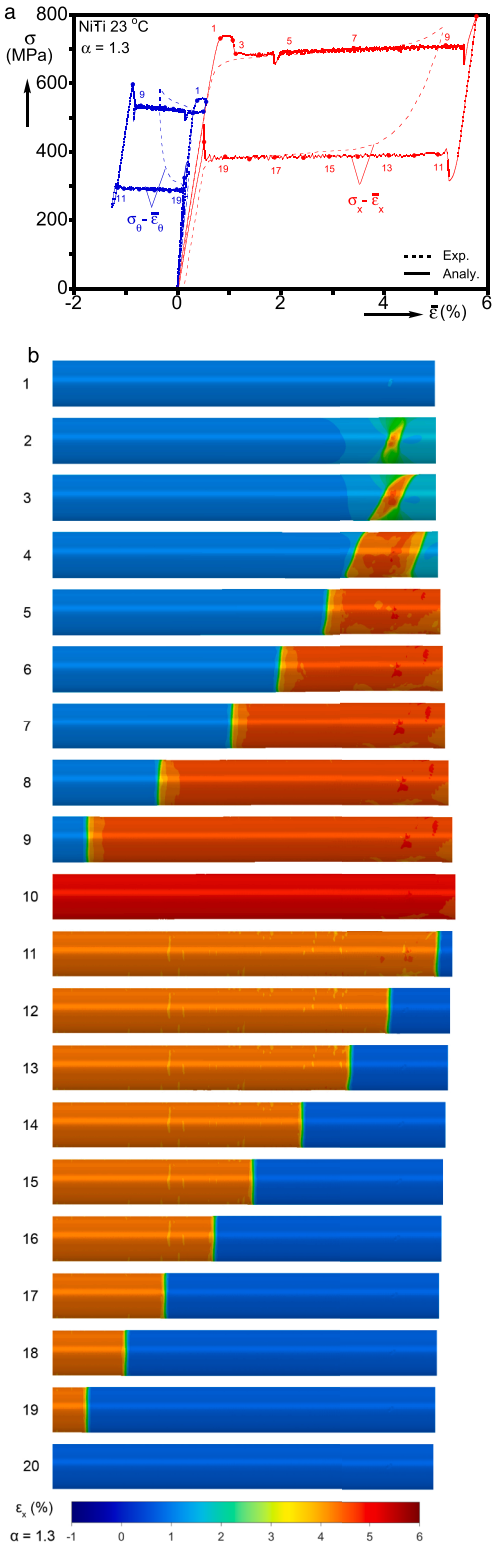

Fig. 22. (a) Calculated and measured stress-average strain responses for biaxial case $\sigma_x = 1.3\sigma_\theta$. (b) Sequence of calculated axial strain contours ($x-z$ plane) corresponding to the numbered bullets marked on the responses in (a).

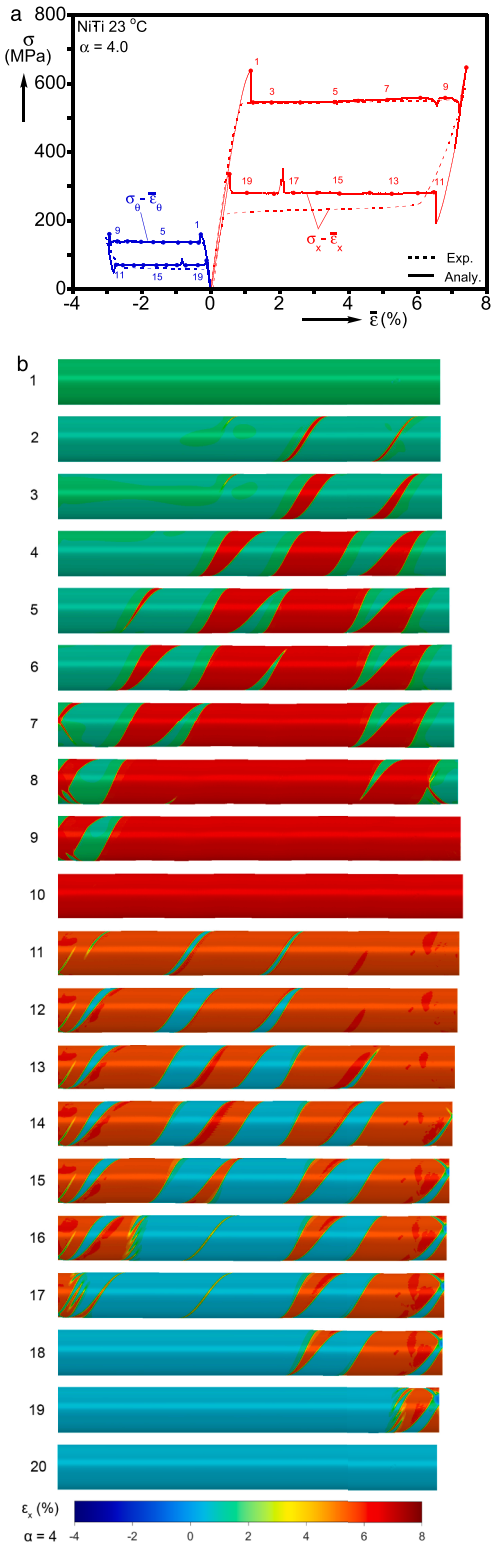

Fig. 23. (a) Calculated and measured stress-average strain responses for biaxial case $\sigma_x = 4.0\sigma_\theta$. (b) Sequence of calculated axial strain contours ($x-z$ plane) corresponding to the numbered bullets marked on the responses in (a).

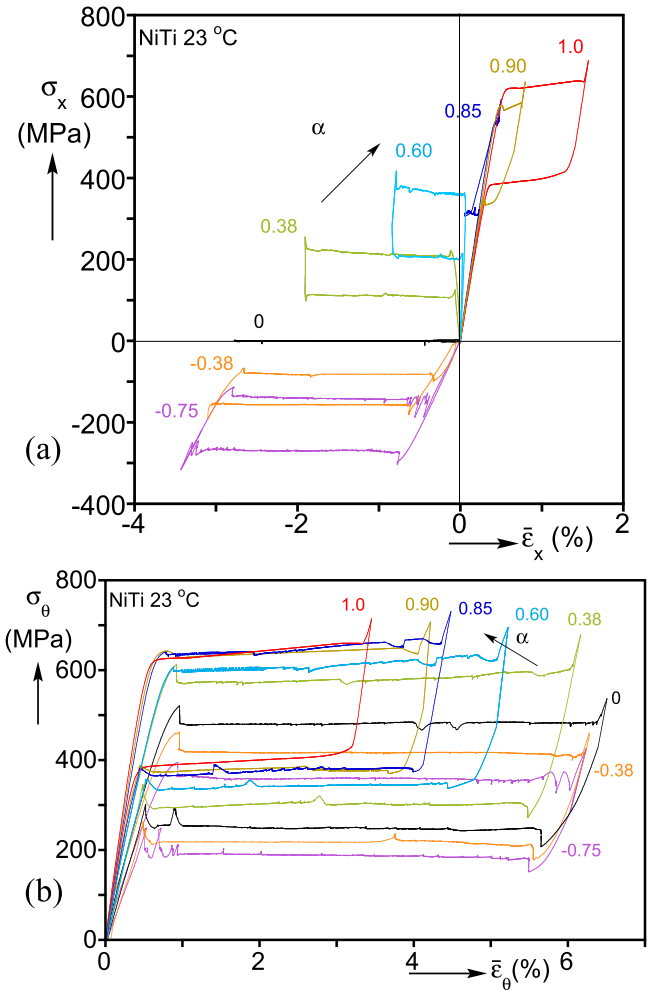

Fig. 24. Calculated and measured stress-average strain responses for biaxial stress states with $\alpha \leq 1.0$: (a) $\sigma_x - \overline{\varepsilon}_x$ and (b) $\sigma_\theta - \overline{\varepsilon}_\theta$.

During unloading deformation remains uniform until station ⑦ on the lower stress branch. The nucleation of the lower strain is not registered on the response and transformation progresses from the left toward the right, with an even more diffuse front that is at 90° to the axis of the tube (see profiles ⑧ and ⑨ in Fig. 20). The amplitudes of moments that develop for this case are small because of the mild and diffuse nature of the deformation patterns that develop, and are not shown.

$\sigma_x = 1.2\sigma_\theta$

As α increases further, the level of axial stress at transformation increases and so does the extent of the axial strain. Correspondingly, both are reduced in the hoop direction. For $\alpha = 1.2$, σ_x at transformation is 666 MPa – the maximum value calculated - which is very close to the measured value, and the two strain extents are nearly the same (see Fig. 21a). By contrast, the experimental hoop strain was close to zero, and the axial hysteresis extended to a larger strain than in the analysis. As for $\alpha = 1.0$, the responses do not exhibit a nucleation peak or valley with the axial stress increasing to 697 MPa by the end of transformation. This relatively mild hardening induces diffuse transformation fronts that are again oriented at 90° to the axis of the tube (Fig. 21b). Transformation initiates on the right end and propagates to the left. Reverse transformation takes place via diffuse fronts also, but here the fronts propagate from left to right. In the experiment transformation produced essentially homogeneous deformation with weak localization patterns in the axial strain that are oriented at 90° to the axis of the tube. The moments are again small and are not reported.

$\sigma_x = 1.3\sigma_\theta$

At the stress ratio of 1.3 the nucleation peak and valley have reappeared and so have the flatter transformation stress plateaus (Fig. 22a). Higher strain initiates as an angled band (Fig. 22b) from the imperfection at an axial stress of 739 MPa. It propagates at about 700 MPa, which matches the experimental plateau. The transformation strain is about 5.5%, whereas in the experiment it was

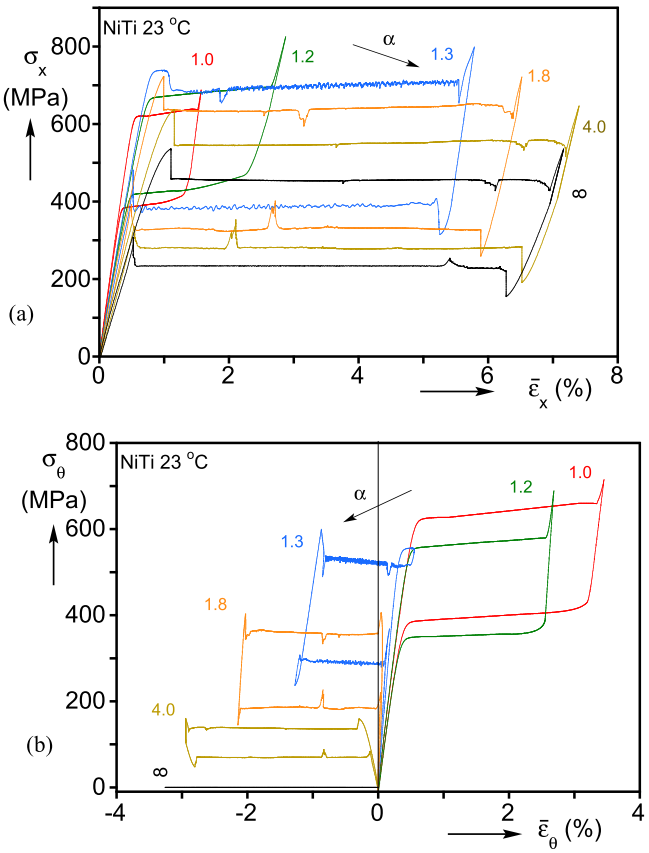

Fig. 25. Calculated and measured stress-average strain responses for biaxial stress states with $\alpha \geq 1.0$: (a) $\sigma_x - \bar{\varepsilon}_x$ and (b) $\sigma_\theta - \bar{\varepsilon}_\theta$.

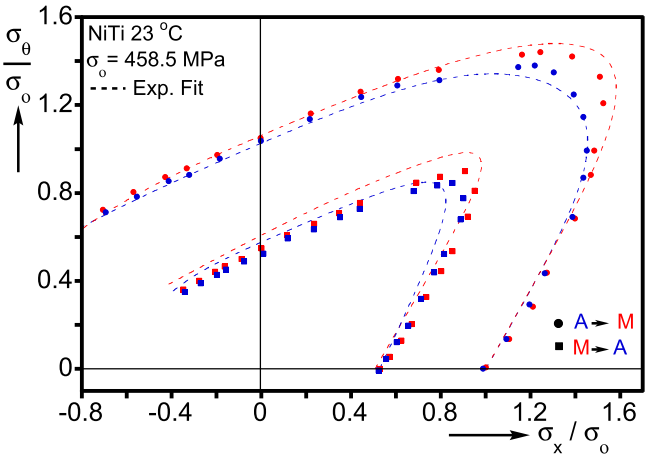

Fig. 26. Loci of calculated stresses at the "nucleation" and "completion" of M and A transformations and fits of the corresponding experimental surfaces from Fig. 27Bechle and Kyriakides, 2016a.

about 4.8%. The hoop stress follows the prescribed ratio, and the Poisson's effect prevails and the hoop strain becomes negative. The initial narrow inclined band develops two angled fronts that propagate in both directions – image ④. The asymmetry of this pattern causes built-up in moments (not shown), which are not sustainable and between stations ④ and ⑤ the band reverts to a 90° orientation relieving the moments for the rest of the simulation. Beyond station ⑤, the 90° front propagates to the left causing small fluctuations in the stresses. The fluctuations are caused by the alignment of the 90° band with the finite element mesh (see Fig. 10). Transformation is completed with a stress valley when the front encounters the left end.

The specimen unloads uniformly down to an axial stress of 313 MPa. Axial strain of about 0.54% initiates at the right end as an

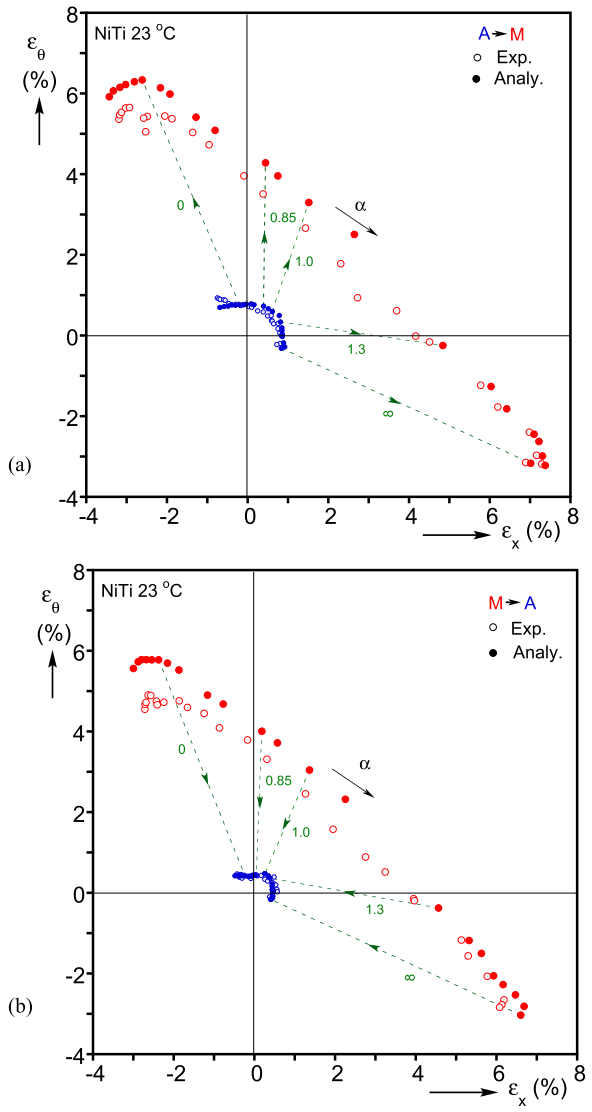

Fig. 27. Calculated axial vs. hoop strains at the "nucleation" and "completion" of: (a) M and (b) A transformations.

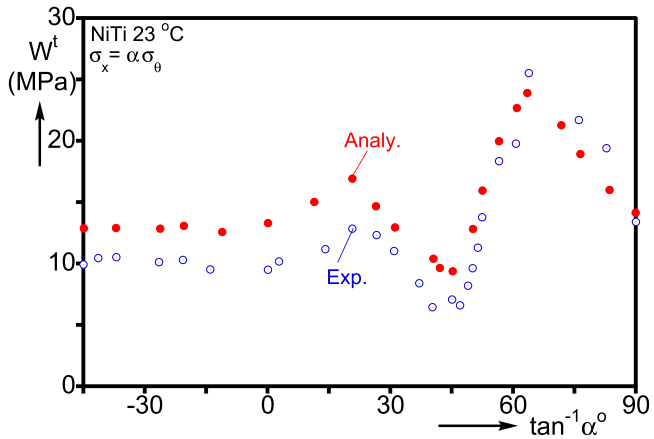

Fig. 28. Calculated and measured transformation dissipation energy vs. stress ratio angle.

angled band that quickly reverts to a 90° front (see image ⑪). The front propagates to the left tracing a plateau of about 390 MPa that matches the experimental value. The stress again fluctuates for the same reason but more moderately because of the lower stress level. The last sliver of high strain on the left end unloads with a spike in the stress.

$\sigma_x = 4.0\sigma_\theta$

Increasing the stress ratio to 4.0 lowers the hystereses and increases their strain extents (Fig. 23a). Thus, the A→M axial stress plateau is at 546 MPa and the induced strain is about 7.2% both matching the experimental values. Strain of about 7.2% in the form of sinistral helical band inclined at 57.6° initiates from the imperfection and is accompanied by a sharp drop in stress (Fig. 23b). In the experiment the band was sinistral with an angle of 60.3°. The band propagates toward the left end broadening in the process. It reaches the left end first and reflects in the opposite direction as shown in image ⑦; the same happens at the right end (image ⑧). The lower strain island on the right transforms first in a snap fashion leading to small stress valleys and the sudden drop in the moment just before station ⑨. By image ⑩ the remaining island of lower strain on the left transforms.

As in most cases, unloading is stiffer than in the experiment. Lower strain nucleates as a sinistral band near the middle of the domain at ⑪ with a sudden increase in axial stress to a plateau level of about 278 MPa, somewhat higher than the measured value. The band propagates in both directions and broadens. The transformation evolves in this manner until it starts to interact with the ends via multi-pronged bands. The left end transforms first in a snap manner, causing spikes in the stresses between stations ⑰ and ⑱. The right end deforms last with the same effects. In contrast to this banded evolution of the reverse transformation of the analysis, the experiment unloaded with primarily multi-pronged fronts similar to those observed axial tension. Overall, the results of this case are representative of axial stress dominant ratios between 1.5 and uniaxial tension ($\alpha = \infty$).

5. Discussion of the results

The analysis has been used to perform 22 simulations of the biaxial response of tubes under stress ratios in the range of $-1 \le \alpha \le \infty$ (16 coincide with the experiments in Bechle and Kyriakides, 2016a). The main characteristics of the results are summarized in Table 2. Figs. 24 and 25 show a select number of the calculated $\sigma_x - \overline{\varepsilon}_x$ and $\sigma_\theta - \overline{\varepsilon}_\theta$ responses for $-0.75 \le \alpha \le 1.0$ and $1.0 \le \alpha \le \infty$ respectively, which correspond to the experimental results in Figs. 25 and 26 of Bechle and Kyriakides (2016a). All cases trace closed hystereses of varying sizes. For stress ratios between −0.75 and 1.0 the hoop hysteresis dominates and for larger values of α the axial hysteresis becomes increasingly more so. In district difference from the experiments, the responses exhibit a stress peak at the nucleation of M and a stress valley at the nucleation of A on unloading – cases 1.0 and 1.2 are exceptions. The relatively unconstrained boundaries of the model allow such features to develop, whereas in the experiments they were masked by the circumferentially clamped ends. Nucleation of the alternate phase leads to localized deformation, mostly in the form of narrow helical bands of higher/lower strain with distinct orientations. The alternate phase spreads along the length of the tube forming distinct patterns while the stresses remain relatively constant – for comparison of calculated and measured deformation patterns see individual cases in Section 4. Overall, the calculated responses reproduce the behavior observed in the experiments quite well.

Figs. 26–29 present a more quantitative overall comparison between the measured and calculated results. Fig. 26 plots the axial against the hoop stresses at the "nucleation" and "completion" of M and A transformations from the 22 cases analyzed. For the best comparison with the measured values, each transformation stress was evaluated from the dominant hysteresis by extrapolating the stress plateau as shown in Fig. C1. The nucleation and completion stresses are designated as $\{\sigma_{iNM}, \sigma_{iCM}\}$ and $\{\sigma_{iNA}, \sigma_{iCA}\}$–Table 2 lists the nucleation stresses of each phase. Included in the figure are the fits of the loci of the corresponding experimental stresses – from Fig. 27 of Bechle and Kyriakides (2016a). Fig. 27 plot the axial versus the hoop strain at the nucleation and completion of M (Fig. 27a)

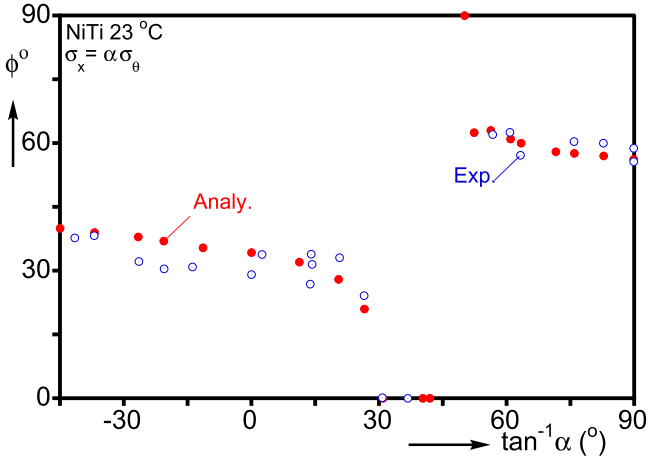

Fig. 29. Calculated and measured inclination of martensitic localization band to axial direction vs. stress ratio angle.

and A (Fig. 27b) together with the experimental data. The radial difference of each pair of strains combines the extents of the transformation strains, listed under $\Delta\varepsilon^t_{xM}$ and $\Delta\varepsilon^t_{\theta M}$ in Table 2.

In agreement with the experiments, as α increases from -0.75 to 1.0 the transformation stresses increase while the transformation strains decrease. Up to stress ratio of 0.5, the responses trace quite flat stress plateaus during both loading and unloading and, as a result, each of the two pairs of stresses are close together. The ones corresponding to the upper plateaus follow the experimental fits very well, while the lower plateau pairs fall somewhat below them. This trend reflects the generally very good prediction of the upper plateaus and the moderate under-prediction of the lower plateaus. For α between 0.6 and 1.0, the responses exhibit modest hardening causing the two transformation stresses to be increasingly further apart. However, since the hardening is milder in the analysis the separation between the nucleation and completion stresses is underestimated.

The strain plots in Fig. 27a quantify the reducing trend of the extent of the transformation strain as α increases from -0.75 to 1.0. The trend is in agreement with that of the experiments, however the magnitudes of extents are over-predicted primarily because the transformation strain of the dominant hoop hysteresis is over-predicted by the analysis. The strain plots of the M→A transformation in Fig. 27b exhibit a similar over-prediction of the extents.

For $\alpha > 1$, the axial stress hysteresis becomes increasingly more dominant and the transformation stresses follow a decreasing trend (Figs. 25 and 26). The hardening exhibited in the neighborhood of $\alpha = 1$ decreases, and for stress ratios larger than 1.3 stress plateaus reappear. Consequently the two pairs of transformation stresses in Fig. 26 come closer together. For loading, their values follow the experimental fits while the separation exhibited for unloading is not captured as accurately. In concert with the experiments, the strain extents grow with α (Fig. 27). Furthermore, since the dominant axial hystereses are reproduced well by the analysis, the extents are much closer to the experimental values.

Fig. 28 plots the energy dissipated by the transformation, W^t (the area enclosed by the hystereses), against $\tan^{-1}\alpha$ together with the experimental values. Overall the calculated values follow the trend of the experiments: for the negative values of α, the energy remains nearly constant; for stress ratios between 0 and 0.375 it has an increasing trend, and drops to a minimum at $\alpha = 1.0$; for values larger than 1.0 the energy increases, achieves a maximum value at 2.0, and decreases again for larger values. For $\alpha \leq 0.375$ the results over-predict W^t, primarily because of the larger extent of the hoop hystereses. The over-estimation continues for $0.375 < \alpha \leq 1.0$ but the difference is smaller. For the axial stress dominant values of $\alpha > 1$, the predicted W^t is generally closer to the measured values. The asymmetric distribution of the dissipated energy about $\alpha = 1.0$ is another manifestation of the asymmetry in the mechanical behavior of this SMA.

Nucleation of M during loading and of A during unloading is mostly in the form of helical bands of higher/lower strain. The band angle ϕ is determined at the nucleation of M and is defined as the inclination of the initial band to the axis of the tube. The values of ϕ are listed in Table 2 and plotted against $\tan^{-1}\alpha$ in Fig. 29 together with the experimental results. The angle starts at 40° at $\alpha = -1$, gradually reduces to 34.3° at $\alpha = 0$, and drops steeply to 0° for stress ratios of 0.6 to 0.9. On the other side of the transformation surface, ϕ starts at 56.2° for pure axial tension, increases to 62.5° at $\alpha = 1.3$ and shoots to 90° at 1.2 and 1.0. It is important to point out that unlike the rest of the simulation results, $\alpha = 1.0$ and 1.2 developed only very weak and diffuse fronts. Thus, the simulations confirm that in the neighborhood of $\alpha = 1.0$ a "dark" zone exists which does not support sharp discontinuities. Presumably this is related to the hardening exhibited by the responses (see predictions of this zone using Hill's (1952) band angle criterion in Fig. 24 of Bechle and Kyriakides, 2016a). The angles at the two uniaxial stress cases, of 34.3° for $\alpha = 0$ and 56.2° for axial tension, differ slightly for the Hill angles of 35.3° and 54.7° respectively, calculated for incompressible and isotropic material. The rest of the angles follow quite well the trend of the experiments but with small differences from individual measurements.

6. Summary and conclusions

Previous work has demonstrated that in the pseudoelastic temperature regime NiTi under uniaxial tension leads to a hysteresis with an upper and a lower stress plateau during which two phases co-exist and deformation is inhomogeneous. Under compression, the hysteresis is monotonic with higher stress, lower strain, and essentially homogeneous deformation. The phenomenological constitutive model developed by our group uses a single surface to describe both forward and reverse transformation, and captures the tension/compression asymmetry by representing uniaxial compression with a hardening potential and uniaxial tension with a partially softening one. The model was implemented in finite element analyses that successfully simulated structural problems primarily under axial stresses. The biaxial experiments of Bechle and Kyriakides (2016a) on thin-walled tubes under combined axial force and internal pressure revealed that in addition to the tension/compression asymmetry the tubular stock exhibited anisotropy.

The present study extended the constitutive model to include anisotropy, calibrated it anew, implemented it in a finite element model, and used a custom incremental loading scheme to simulate the biaxial experiments over a range of biaxiality stress ratios. By and large, the simulations capture the main features of the experimental results. Following are some general trends, observations, and areas of potential improvements.

- The stress-average strain responses are reproduced quite well for nearly the whole range of biaxiality stress ratios considered ($-1 \leq \alpha \leq \infty$).
- Excluding a zone around the equibiaxial stress ratio, the biaxial responses trace stress plateaus and inhomogeneous deformation during transformation in the form of spiral and multipronged patterns.
- In the neighborhood of $\alpha = 1$, the hystereses are nearly monotonic and the deformation is nearly homogeneous.

- The mild anisotropy exhibited by the transformation stresses is captured well. The anisotropy in the extents of the stress plateaus is over-predicted for hoop dominant stress paths, primarily because the extent of pure hoop stress hysteresis was somewhat over-predicted by the form of anisotropy adopted. This is also responsible for the larger transformation energy predicted for $\alpha \leq 1.0$. The predicted extents of the axial stress dominant paths ($\alpha > 1.2$) are closer to the measured values and so is the transformation energy.
- The monotonicity of the responses in the neighborhood of $\alpha = 1$ is strongly governed by the hardening behavior exhibited under uniaxial compression. The relatively simple two-parameter anisotropy adopted resulted in a lower hardening than measured. This in turn led to lower hardening in the calculated responses for biaxiality ratios close to $\alpha = 1$, and caused slight deviations in the separation of the transformation stresses. We expect that a more extensive representation of anisotropy can alleviate these minor deviations of the analysis from the experimental results.
- The spiral angles at the onset of transformation follow the trend of the measured values including the "dark" zone in the neighborhood of $\alpha = 1$. This demonstrates the importance of both tension/compression asymmetry as well as that of the anisotropy in reproducing the experimental results.

In closing, we reiterate that the present form of the constitutive model is “local” and the usual regularization resulting from the introduction of rate is not provided by the constitutive model framework adopted. An alternative approach is to introduce higher order gradients in the formulation, which has an associated length scale that must be provided. This results in a significant increase in the computational time. Instead, the uniform mesh adopted was chosen for optimal reproduction of the finer localization features reported in the experiments. Mesh sensitivity studies demonstrated that, as in our previous works, the mesh does not influence the overall structural response or the patterns significantly. Its main effect is limited to controlling the width of the transition separating transformed and untransformed zones.

Declaration of Competing Interest

The authors declare that they have no known competing financial interests or personal relationships that could have appeared to influence the work reported in this paper.

Acknowledgments

The authors acknowledge with thanks the financial support received for this work from the National Science Foundation under grant no. CMMI-1762389. The literature on Shape Memory Alloys is vast and as a result we have limited citations to papers that directly impact our work. Special thanks go to Dongjie Jiang for help in the implementation of the original constitutive model UMAT.

Appendix A. Uniaxial Stress States

The following derivatives are required in (14):

$$\frac{\partial J'_2}{\partial \varepsilon^t_{ij}} = \frac{2}{3}\frac{e^t_{ij}}{J'_2}, \tag{A1}$$

$$\frac{\partial \widetilde{J}'_2}{\partial \varepsilon^t_{ij}} = \frac{2}{3}\frac{\widetilde{e}_{ij}{}^t}{\widetilde{J}'_2}, \tag{A2}$$

$$\frac{\partial \widetilde{J}'_3}{\partial \varepsilon^t_{ij}} = \frac{4}{3}\frac{D_{klij}}{\widetilde{J}'^2_3}\left(\frac{1}{2}\delta_{mk}\delta_{nl} + \frac{1}{2}\delta_{ml}\delta_{nk} - \frac{1}{3}\delta_{mn}\delta_{kl}\right)\widetilde{e}^t_{np}\,\widetilde{e}^t_{pm}, \tag{A3}$$

$$\frac{\partial \widetilde{J}'_r}{\partial \varepsilon^t_{ij}} = \frac{\partial}{\partial \varepsilon^t_{ij}}\left(\frac{\widetilde{J}'_3}{J'_2}\right) = -\frac{\widetilde{J}'_3}{J'^2_2}\frac{\partial J'_2}{\partial \varepsilon^t_{ij}} + \frac{\partial \widetilde{J}'_3}{J'_2 \partial \varepsilon^t_{ij}}, \tag{A4}$$

$$\frac{\partial \widetilde{\varepsilon}^t_e}{\partial \varepsilon^t_{ij}} = f(\widetilde{J}'_r)\frac{\partial \widetilde{J}'_2}{\partial \varepsilon^t_{ij}} + \widetilde{J}_2{}'\frac{df}{d\widetilde{J}'_r}\frac{\partial \widetilde{J}'_r}{\partial \varepsilon^t_{ij}}. \tag{A5}$$

Specializing these to the uniaxial stretch, $\varepsilon^t = \{\varepsilon^t_{11}, \varepsilon^t_{22}, \varepsilon^t_{33}\} = \varepsilon_o\{1, -1/2, -1/2\}$ leads to

$$J_2{}' = |\varepsilon_o|, \widetilde{J}_2{}' = |\varepsilon_o|,\ \widetilde{J}'_3 = \varepsilon_o,\ \widetilde{J}_r{}' = \mathrm{sgn}(\varepsilon_o),\ \widetilde{\varepsilon}^t_e = |\varepsilon_o| f(\mathrm{sgn}(\varepsilon_o)) \tag{A6}$$

$$\frac{\partial \widetilde{J}'_r}{\partial \varepsilon^t_{11}} = 0,\ \frac{\partial \widetilde{\varepsilon}^t_e}{\partial \varepsilon^t_{11}} = \mathrm{sgn}(\varepsilon_o)\frac{2}{3}f(sgn(\varepsilon_o)). \tag{A7}$$

Similarly for uniaxial stretch in the other two directions:

$$\varepsilon_o\{-1/2, 1, -1/2\} \; and \; \varepsilon_o\{-1/2, -1/2, 1\}$$

$$J_2{}' = |\varepsilon_o|, \widetilde{J}_2{}' = \gamma|\varepsilon_o|, \widetilde{J}_3{}' = \beta\varepsilon_o, \; \widetilde{J}_r{}' = \beta\mathrm{sgn}(\varepsilon_o), \; \widetilde{\varepsilon}_e^t = \gamma|\varepsilon_o| f(\mathrm{sgn}(\varepsilon_o)) \tag{A8}$$

$$\frac{\partial \widetilde{J}_r{}'}{\partial \varepsilon_{22}^t} = \frac{\partial \widetilde{J}_r{}'}{\partial \varepsilon_{33}^t} = 0, \quad \frac{\partial \widetilde{\varepsilon}_e^t}{\partial \varepsilon_{22}^t} = \frac{\partial \widetilde{\varepsilon}_e^t}{\partial \varepsilon_{33}^t} = \gamma \mathrm{sgn}(\varepsilon_o) \frac{2}{3} f(\beta \mathrm{sgn}(\varepsilon_o)) \tag{A9}$$

Appendix B. Calibration of Anisotropy

One manifestation of the anisotropy is the significant difference between the axial and hoop tensile stress–strain responses reported in Fig. 2a. Fig. B1a shows a first attempt at correcting this by introducing a single anisotropy parameter $A_1 = A_2$. Plotted is the calculated $\sigma_\theta - \varepsilon_\theta$ response for various values of this variable (for simplicity only the loading half of the calculated response is shown). The value 1.0 corresponds to the isotropic case. The up-down-up calibration response is based on the measured tensile response in the θ-direction ($\alpha = 0$) and consequently extends to a much higher hoop strain than required. Reducing this variable reduces the strain extent but also moves the response to a higher stress level. To address these issues, in Fig. B2a A_2 is kept at the seemingly optimal value of 0.93 while A_1 is varied independently. Reducing A_1 moves the stress level back down and extends the response to a smaller strain than in the previous attempt. Results in a similar plot Fig. B2b were obtained by fixing $A_1 = 0.88$ and varying A_2. Increasing A_2 progressively from 0.88 moves the response to lower stress level and at the same time extends it to some degree. Through this iterative process $A_1 = 0.88$ and $A_2 = 0.93$ were found to produce an acceptable compromise in the stress level and strain extents for this experiment.

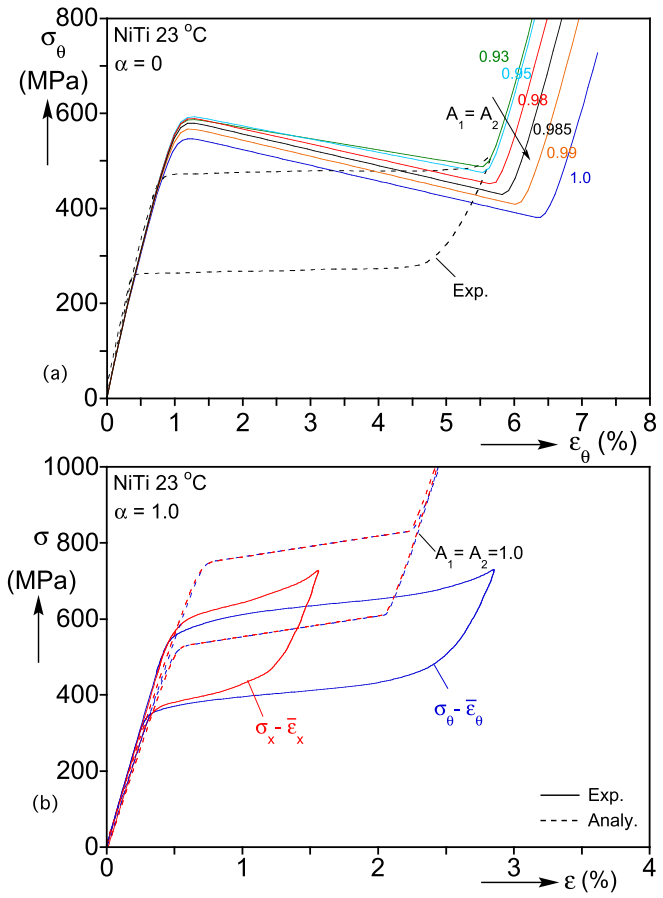

Fig. B1. (a) Up-down-up representation of the pure hoop stress response for various values of the anisotropy parameter $A_1 = A_2$. (b) Model representation of the tension/compression asymmetry exhibited in the equibiaxial responses, $\alpha = 1.0$, without anisotropy ($A_1 = A_2 = 1$).

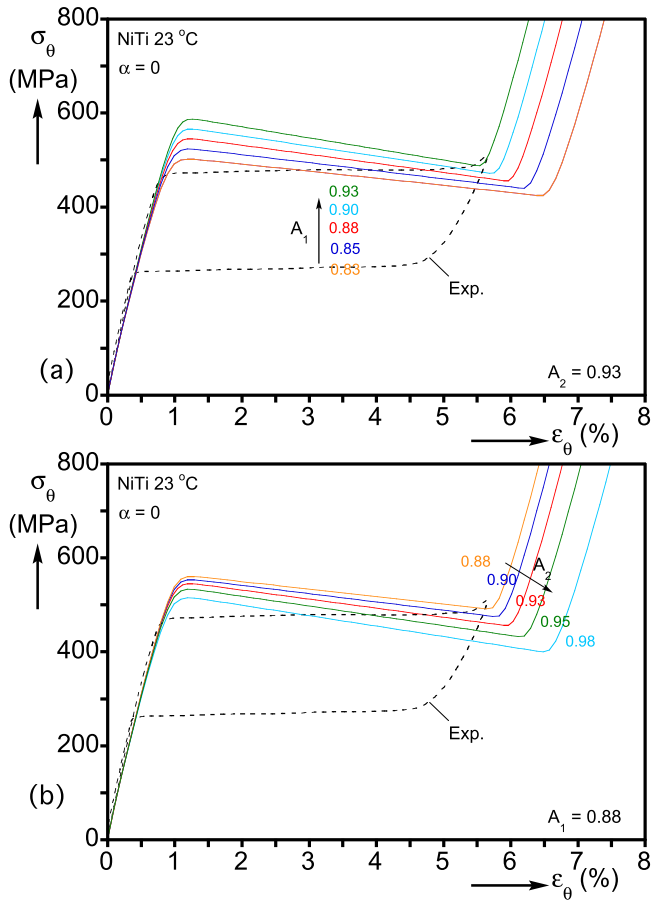

Fig. B2. Up-down-up representation of the pure hoop stress response for various values of the anisotropy parameters: (a) A_1 with $A_2 = 0.93$ and (b) A_2 with $A_1 = 0.88$.

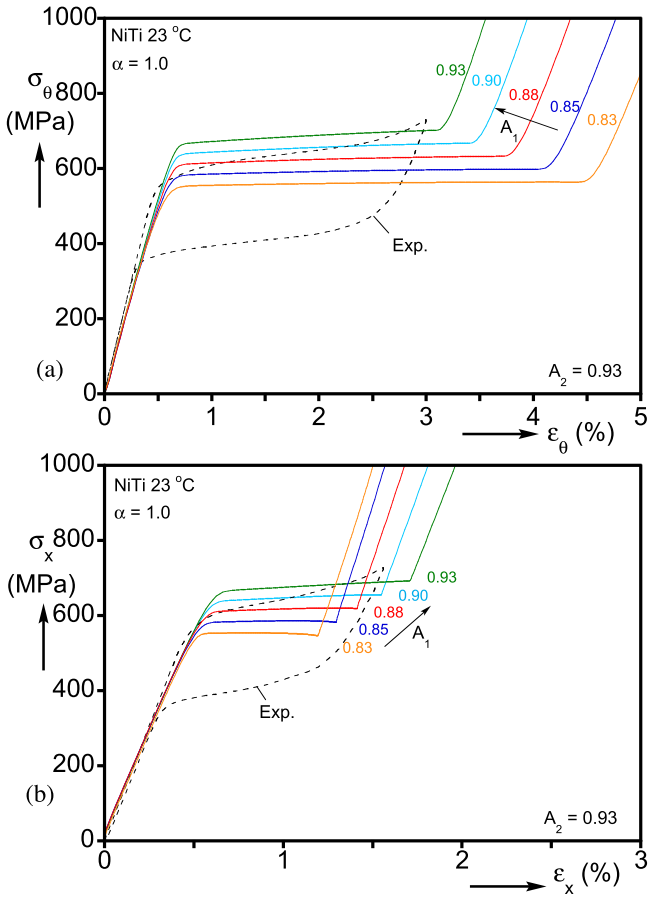

Fig. B3. Hardening representation of the equibiaxial responses for various values of the anisotropy parameter A_1 with $A_2 = 0.93$: (a) hoop and (b) axial results.

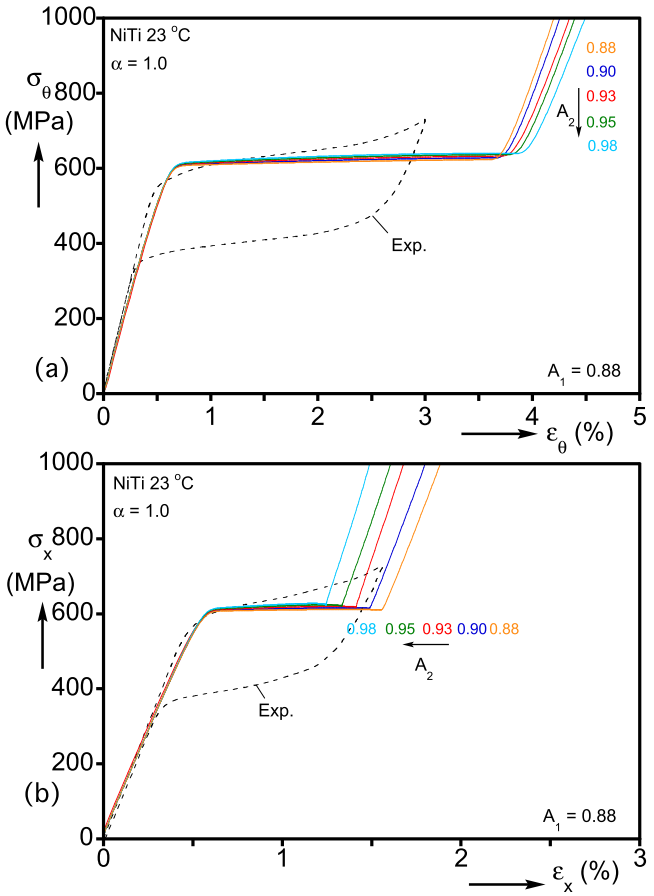

Fig. B4. Hardening representation of the equibiaxial responses for various values of the anisotropy parameter A_2 with $A_1 = 0.88$: (a) hoop and (b) axial results.

A second consequence of anisotropy is illustrated of in Fig. B1b, which plots the measured axial and hoop direction responses for the equibiaxial $(\sigma_x = \sigma_\theta)$ radial path. This stress state can be viewed as equivalent to uniaxial compression in the third principal direction. In the absence of any anisotropy, the model predicts equal responses in the two directions, which trace higher stress and strains with extents that differ from those measured. Thus, the effect of the two anisotropy parameters on these responses were examined in parallel with the effect on the pure hoop stress experiment discussed above. Fig. B3 shows the predictions for the x and θ responses for the same range of A_1 values with $A_2 = 0.93$ as in Fig. B2a. All variables considered produce monotonically increasing responses with various stress levels and strain extents. The optimal value of $A_1 = 0.88$ overpredicts the extent of ε_θ and underpredicts the extent of ε_x with both stress levels being closer to the measurements. Fig. B4 shows similar predictions for the same range of values of A_2 as in Fig. B2b and $A_1 = 0.88$. Increasing A_2 has limited effect on the hoop response but it reduces the axial strain extent maintaining the same stress level. The present way of introducing anisotropy is limited by its coupling to the scaling function through which tension/compression asymmetry is introduced (Eq. (11)). Better representation of the anisotropy may require its decoupling from such a scaling function.

Appendix C. Transformation Stress and Strain

The calculated stress-average strain responses exhibit stress peaks and valleys at the nucleation and completion of transformation. In the experiments these features were masked by the circumferentially clamped boundaries. Accordingly, the stresses at the "nucleation" and "completion" of transformation were determined using "tangent" construction lines as shown in Fig. A1 of Bechle and Kyriakides (2016a). To accommodate a more direct comparison between the calculated and measured critical stresses, the former were determined by the "perceived" beginning and end of the stress plateaus in the absence of the peaks and valley as shown in Fig. C1. Furthermore, the extent of each stress plateau was taken as the strain between the two critical stresses.

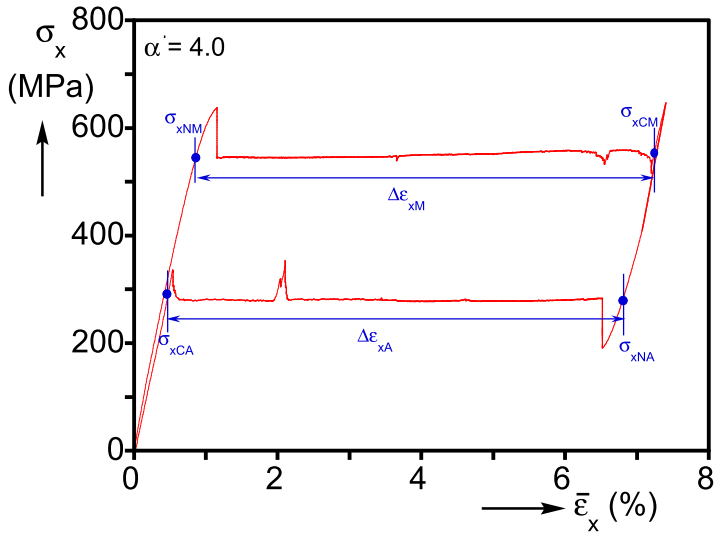

Fig. C1. Definition of the "nucleation" and "completion" stresses of M and A transformations. The strain difference between the two critical stresses is the extent of each transformation.

Supplementary materials

Supplementary material associated with this article can be found, in the online version, at doi:10.1016/j.ijplas.2021.103179.

References

Abeyaratne, R., Knowles, J.K., 2006. Evolution of Phase Transformations: A Continuum Theory. Cambridge University Press, New York. https://doi.org/10.1017/CBO9780511547133.

Bechle, N.J., Kyriakides, S., 2014. Localization in NiTi tubes under bending. Int. J. Solids Struct. 51, 967–980. https://doi.org/10.1016/j.ijsolstr.2013.11.023.

Bechle, N.J., Kyriakides, S., 2016a. Evolution of localization in pseudoelastic NiTi tubes under biaxial stress states. Int. J. Plast. 82, 1–31. https://doi.org/10.1016/j.ijplas.2016.01.017.

Bechle, N.J., Kyriakides, S., 2016b. Evolution of phase transformation fronts and associated thermal effects in a NiTi tube under a biaxial stress state. Extreme Mech. Lett. 8, 55–63. https://doi.org/10.1016/j.eml.2016.02.018.

Daly, S., Ravichandran, G., Bhattacharya, K., 2007. Stress-induced martensitic phase transformation in thin sheets of Nitinol. Acta Mater. 55, 3593–3600. https://doi.org/10.1016/j.actamat.2007.02.011.

Elibol, C., M.F.-X, Wagner, M.F.-X, 2015. Investigation of the stress-induced martensitic transformation in pseudoelastic NiTi under uniaxial tension, compression and compression-shear. Mater. Sci. Eng. A 621, 76–81. https://doi.org/10.1016/j.msea.2014.10.054.

Ericksen, J.L., 1975. Equilibrium of bars. J. Elast. 5, 191–201. https://doi.org/10.1007/BF00126984.

Frost, M., Benešová, B., Seiner, H., Kružík, M., Šittner, P., Sedlák, P., 2021. Thermomechanical model for NiTi-based shape memory alloys covering macroscopic localization of martensitic transformation. Int. J. Solids Struct. 221, 117–129. https://doi.org/10.1016/j.ijsolstr.2020.08.012.

Hallai, J.F., Kyriakides, S., 2011. On the effect of Lüders bands on the bending of steel tubes: part II analysis. Int. J. Solids Struct. 48, 3285–3294. https://doi.org/10.1016/j.ijsolstr.2011.07.012.

Hallai, J.F., Kyriakides, S., 2013. Underlying material response for Lüders-like instabilities. Int. J. Plast. 47, 1–12. https://doi.org/10.1016/j.ijplas.2012.12.002.

Helm, D., Haupt, P., 2001. Thermomechanical behavior of shape memory alloys. In: Proceedings of the SPIE International Symposium Smart Structures and Materials, 8, pp. 302–313. https://doi.org/10.1117/12.432769.

Hill, R., 1952. On discontinuous plastic states, with special reference to localized necking in thin sheets. J. Mech. Phys. Solids 1, 19–30. https://doi.org/10.1016/0022-5096(52)90003-3.

Iadicola, M.A., Shaw, J.A., 2002. An experimental setup for measuring unstable thermo-mechanical behavior of shape memory alloy wire. J. Int. Mater. Syst. Struct. 13, 157–166. https://doi.org/10.1177/104538902761402558.

Jacobus, K., Sehitoglu, H., Balzer, M., 1996. Effect of stress state on the stress-induced martensitic transformation of polycrystalline Ni-Ti Alloy. Metall. Mater. Trans. A 27, 3066–3073. https://doi.org/10.1007/BF02663855.

Jiang, D., Bechle, N., Landis, C.M., Kyriakides, S., 2016a. Buckling and recovery of NiTi tubes under axial compression. Int. J. Solids Struct. 80, 52–63. https://doi.org/10.1016/j.ijsolstr.2016.07.003.

Jiang, D., Landis, C.M., Kyriakides, S., 2016b. Effects of tension/compression asymmetry on the buckling and recovery of NiTi tubes under axial compression. Int. J. Solids Struct. 100-101, 41–53. https://doi.org/10.1016/j.ijsolstr.2016.07.003.

Jiang, D., Landis, C.M., 2016. A constitutive model for isothermal pseudoelasticity coupled with plasticity. Shape Mem. Superelast. 2, 360–370. https://doi.org/10.1007/s40830-016-0078-8.

Jiang, D., Kyriakides, S., Landis, C.M., 2017a. Propagation of phase transformation fronts in pseudoelastic NiTi tubes under uniaxial tension. Extreme Mech. Lett. 15, 113–121. https://doi.org/10.1016/j.eml.2017.06.006, 2017.

Jiang, D., Kyriakides, S., Bechle, N.J., Landis, C.M., 2017b. Bending of pseudoelastic NiTi tubes. Int. J. Solids Struct. 124, 192–214. https://doi.org/10.1016/j.ijsolstr.2017.06.032.

Jiang, D., Kyriakides, S., Landis, C.M., Kazinakis, K., 2017c. Modeling of propagation of phase transformation fronts in NiTi under uniaxial tension. Euro. J. Mech. A/Solids 64, 131–142. https://doi.org/10.1016/j.euromechsol.2017.02.004.

Kazinakis, K., Kyriakides, S., Jiang, D., Bechle, N.J., Landis, C.M., 2021. Buckling and collapse of pseudoelastic NiTi tubes under bending. Int. J. Solids Struct. 221, 2–17. https://doi.org/10.1016/j.ijsolstr.2019.12.017.

Kazinakis, K., 2022. Localization instabilities in pseudoelastic NiTi tubes under multiaxial stress states, PhD Dissertation, The University of Texas at Austin.
Kyriakides, S., Miller, J.E., 2000. On the propagation of Lüders bands in steel strips. ASME J. Appl. Mech. 67, 645–654. https://doi.org/10.1115/1.1328348.
Landis, C.M., 2003. On the strain saturation conditions for polycrystalline ferroelastic materials. ASME J. Appl. Mech. 70, 470–478. https://doi.org/10.1115/1.1600472.
Li, Z.Q., Sun, Q.P., 2002. The initiation and growth of macroscopic martensite band in nano-grained NiTi microtube under tension. Int. J. Plast. 18, 1481–1498. https://doi.org/10.1016/S0749-6419(02)00026-8.
Liu, Y., Hoover, I., Xiang, H., Bataillard, L., Miyazaki, S., 1999. Strain dependence of pseudoelastic hysteresis of NiTi. *Metal. Mater. Trans*. 30A, 1275–1282. https://doi.org/10.1007/s11661-999-0276-5.
Mao, S., Luo, J., Zhang, Z., Wu, M., Liu, Y., Han, X., 2010. EBSD studies of the stress-induced B2-B19′ martensitic transformation in NiTi tubes under uniaxial tension and compression. Acta Mater. 58, 3357–3366. https://doi.org/10.1016/j.actamat.2010.02.009.
Orgéas, L., Favier, D., 1998. Stress-induced martensitic transformation of a NiTi alloy in isothermal shear, tension and compression. Acta Mater. 46, 5579–5591. https://doi.org/10.1016/S1359-6454(98)00167-0.
Reedlunn, B., Churchill, C.B., Nelson, E.E., Shaw, J.A., Daly, S.H., 2014. Tension, compression, and bending of superelastic shape memory tubes. J. Mech. Phys. Solids 63, 506–537. https://doi.org/10.1016/j.jmps.2012.12.012.
Reedlunn, B., LePage, W.S., Daly, S.H., Shaw, J.A., 2020. Axial-torsion behavior of superelastic tubes: part I, proportional isothermal experiments. Int. J. Solids Struct. 199, 1–35. https://doi.org/10.1016/j.ijsolstr.2020.03.018.
Rezaee-Hajidehi, M., Stupkiewicz, S., 2021. Modelling of propagating instabilities in pseudoelastic NiTi tubes under combined tension–torsion: helical bands and apparent yield locus. Int. J. Solids Struct. 221, 130–149. https://doi.org/10.1016/j.ijsolstr.2020.09.011.
Sedlak, P., Frost, M., Benešova, B., Ben Zineb, T., Šittner, P., 2012. Thermomechanical model for NiTi-based shape memory alloys including R-phase and material anisotropy under multi-axial loadings. Int. J. Plast. 39, 132–151. https://doi.org/10.1016/j.ijplas.2012.06.008.
Shaw, J.A., Kyriakides, S., 1995. Thermomechanical aspects of NiTi. J. Mech. Phys. Solids 43, 1243–1281. https://doi.org/10.1016/0022-5096(95)00024-D.
Shaw, J.A., Kyriakides, S., 1997. On the nucleation and propagation of phase transformation fronts in a NiTi alloy. Acta Mater. 45, 683–700. https://doi.org/10.1016/S1359-6454(96)00189-9.
Shaw, J.A., Kyriakides, S., 1998. Initiation and propagation of localized deformation in elasto-plastic strips under uniaxial tension. Int. J. Plast. 13, 837–871. https://doi.org/10.1016/S0749-6419(97)00062-4.
Sun, Q.P., Li, Z.Q., 2002. Phase transformation in superelastic NiTi polycrystalline micro-tubes under tension and torsion—from localization to homogeneous deformation. Int. J. Solids Struct. 39, 3797–3809. https://doi.org/10.1016/S0020-7683(02)00182-8.
Yu, C., Kang, G., Kan, Q., Zhu, Y., 2015. Rate-dependent cyclic deformation of super-elastic NiTi shape memory alloy: thermo-mechanical coupled and physical mechanism-based constitutive model. Int. J. Plast. 72, 60–90. https://doi.org/10.1016/j.ijplas.2015.05.011.